Master's thesis

NTNU
Norwegian University of Science and Technology
Faculty of Natural Sciences
Department of Physics

Mats-Johan Hagen Fagerheim

Time Resolved X-ray μCT studies of Multiphase Flow in Porous Systems

Master's thesis in physics and mathematics
Supervisor: Ragnvald Mathiesen and Amir Ghaderi
July 2023

NTNU
Norwegian University of Science and Technology

SINTEF

Mats-Johan Hagen Fagerheim

Time Resolved X-ray μCT studies of Multiphase Flow in Porous Systems

Master's thesis in physics and mathematics
Supervisor: Ragnvald Mathiesen and Amir Ghaderi
July 2023

Norwegian University of Science and Technology
Faculty of Natural Sciences
Department of Physics

NTNU
Norwegian University of
Science and Technology

Abstract

X-ray micro computed tomography was utilised to conduct an in-situ study of a multiphase flow involving paraffin and air within a 3D-printed porous media composed of Epoxy Resin. A series of 57 sequential tomograms were acquired at 1-minute intervals, with each acquisition lasting 40 seconds. The resulting dataset provided insights into the motion of the fluids and the morphological evolution of the paraffin-air interface as paraffin was drained from the system.

A velocity analysis of the paraffin-air interface was conducted by fitting well-defined mathematical surfaces to specific regions of the interface. The velocities derived from these surfaces were measured at the scale of micrometre per minute with a maximum measured velocity of 58 µm/min. On the basis of these velocities, it was concluded that the fluid interface was not fully resolved spatiotemporally but only for some regions of the system. Despite this, the experiment was able to capture the general development of the system, which was shown to be most affected by the pore morphology, the pump rate, and the wetting properties of the synthetic porous material.

Sammendrag

Røntgen mikro computertomografi har blitt anvendt i et in situ studie av et flerfase strømmings-forsøk bestående av parafin og luft inne i et 3D-printet porøst medium bestående av Epoxy Resin. En serie av 57 sekvensielle tomogram ble innhentet med 1 minutts intervaller hvor selve bildeinnhentingstiden var på 40 sekunder. Det resulterende datasettet gav innsikt i hvordan fluidene beveget seg og hvordan grensesnittet mellom parafin og luft endret seg mens parafin ble pumpet ut av systemet.

En hastighetsanalyse av grenseovergangen mellom parafin of luft ble gjennomført ved å tilpasse veldefinerte matematiske overflater til bestemte områder ved grenseovergangen. Hastighetene som ble hentet ut fra analysen var i mikrometer per minutt skalaen, hvor den maksimale hastigheten ble målt til 58 µm/min. Basert på disse hastighetene ble det konkludert at datasettet ikke var fullt spatiotemporalt oppløst, men kun for bestemte områder av systemet. Til tross for dette klarte forsøket å fange den generelle utviklingen til systemet, som tilsynelatende var mest påvirket av pore-morfologien, pumpen raten og fukt egenskapene til det syntetiske porøse mediet.

Preface

This master's thesis is the final milestone of my five-year physics and mathematics engineering degree and was written in the spring of 2023 under the supervision of Ragnvald Mathiesen from NTNU and Amir Ghaderi from Sintef Industry, amounting to a total of 30 ECTS credits. The objective of the thesis has been to study the feasibility of using X-ray µCT home lab equipment for time-resolved imaging, testing its capabilities in capturing the dynamic change of multiphase flow. This has been a pilot project at Sintef Industri and a source of new ideas and projects. In the true spirit of experimental physics, various approaches have been explored, and numerous challenges and setbacks have been encountered before arriving at the final results presented in this thesis. Luckily, I have been blessed with two very supportive supervisors. They have guided me through this journey with great interest and enthusiasm, providing me with the right tools for success. Without their assistance, completing this thesis would not have been possible. I would also like to express my appreciation to Ole Støren, whose contributions significantly aided in developing the experimental pump used in this research. Furthermore, I would like to extend my thanks to all the employees at Sintef Industri, with whom I had the opportunity to exchange thoughts and engage in discussions during the spring. Lastly, I would like to thank friends and family who have supported me throughout these five years. Their belief in my abilities has been a constant source of motivation.

Disclaimer

This thesis is based on and is a natural continuation of my project thesis titled "Optimizing X-ray computed tomography for the Study of fluid flow in porous media: A analysis of projection number and resolution", written in the autumn of 2022[1], which amounted to 15 ECTS credits. While significant revisions and changes have been made to the text, some structural and textual similarities inevitably exist. These similarities primarily exist in the introduction and theory sections.

Contents

Chapter 1

Introduction

The study of porous media is a complex and important topic, where an enhanced fundamental understanding of it is essential for many fields such as reservoir engineering, soil science, and chemical engineering[2,3]. It becomes increasingly complex when adding multiphase flows into the system, a subject with many important technical applications[3]. CO_2 storage, frost heaving, or drug delivery in patients are all examples of topics related to fluid flow in porous networks[4–6]. The diversity of these examples emphasises the importance of expanding our knowledge within the field.

To be able to study multiphase flow in porous media in an experimental setting, one needs to deal with **1)** The spatial scale at which the governing physics acts often resides the sub-micron level. **2)** The fluid velocities, which despite the small dimensionalities of the porous network, may span several orders of magnitude, and lastly, **3)** the fact that the system is embedded in a solid, often optically opaque[7].

An obvious candidate for such a purpose is X-ray micro Computed Tomography, µCT, a noninvasive imaging technique initially designed to image the static inner structure of an object by collecting a set of projections, hence radiographs, and reconstructing it to form 2D cross-section images of the object, hence a tomogram[8]. In a dynamic setting, each µCT-scan results in a tomogram representing the time-averaged state of the system[9], and despite a high spatial resolution and contrast, the imaging acquisition time is often inadequate to provide the temporal resolutions required for imaging of multiphase flow in the pore network[10,11]. Therefore, it is necessary to optimise the imaging process and to reduce the acquisition time with acceptable compromises in terms of losses in spatial resolution[12]. In addition, it is imperative to customise the experimental setups to regulate the fluid velocities to a scale that can match the acquisition time. This will push the limits of the µCT imaging technique toward achieving the ultimate time-space resolution obtained by more expensive and less accessible experimental setups using a synchrotron as a radiation source[13].

Previous work using CT to study dynamical systems shows that the key is finding a trade-off between contrast, spatial resolution and temporal resolution[11,12]. A priori knowledge obtained from a high spatial resolution tomogram of the object in

a static state provides critical information regarding the system's inner structure. This information, which remains largely unaffected upon introducing fluids, allows for an increased temporal resolution by reducing the acquisition time, in a trade-off with some of the spatial resolution as most of the system then is known. In addition, a priori knowledge of the system can ease some of the problems related to localising and segregating the fluids in the system, which would typically occur with a low-resolution tomogram[14].

This thesis aims to study the multiphase flow of paraffin and air in a simplified porous network model using an µCT-scanner to acquire a sequence of tomograms as the system evolves. Additionally, a high-resolution tomogram of the model, without any fluids in the system, will be acquired. By slowly draining paraffin from the pores, a high contrast dynamical interface is created with the air entering the system. The high contrast boundary will be the subject of the analysis focusing on its temporal development.

This experiment capitalises on an earlier work, "Optimizing X-ray computed tomography for the Study of fluid flow in porous media: A analysis of projection number and resolution."[1], which studied the same pore network used for this experiment and the effects of reducing the number of projections used to reconstruct a tomogram. The results indicated that using 85 projections to reconstruct a tomogram gave the best trade-off between resolution and a low number of projections. However, the findings also suggested that 80 projections could be sufficient, and this reduced number of projections will be used in the current study to prioritise acquisition speed.

Chapter 2

Theory

The theory in the following chapters will primarily be based on the information gathered from the books "Industrial X-ray computed tomography" by Carmignato, Dewulf and Leach, and "Computed tomography" by Buzug[15,16].

2.1 Overview

X-ray Computed Tomography, CT, is a natural extension of conventional X-ray transmission imaging (radiography). The technique computationally reconstructs a set of cross-sectional images of an object by capturing multiple radiograms from different angles of the object. In terms of CT, these radiograms are referred to as projections. In addition to the imaged object, the main element of the CT setup is the X-ray source and the detector. These elements are highlighted in Fig. 2.1, which shows a simple schematic of a typical in-house CT setup and defines the coordinate system used throughout this chapter.

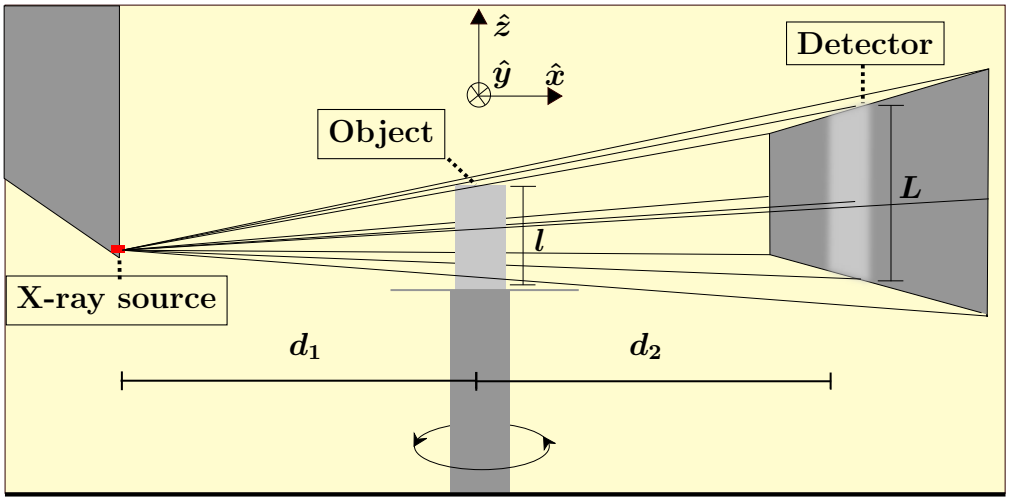

Figure 2.1: Schematic of an X-ray CT setup and its three main elements; the X-ray source, an object placed on a rotating stage and a detector.

Fig. 2.1 illustrates X-rays emitted in a cone beam geometry, which is most common in an in-house CT system as it gives a full 2D projection of the imaged object, and advantageously gives a geometrical magnification, m, of the object onto the detector. The resulting magnification is expressed as

$$m = \frac{L}{l} = \frac{d_1 + d_2}{d_1}, \tag{2.1}$$

where d_1 is the distance from the source to the object, with size l, and d_2 is the distance from the object to the detector, and the size of the image of the object on the detector is L.

2.2 X-ray source

From an optical point of view, the X-ray source is fully characterised by its size, divergence and spectral radiance. The underlying mechanism that generates the X-ray source is illustrated in Fig. 2.2.

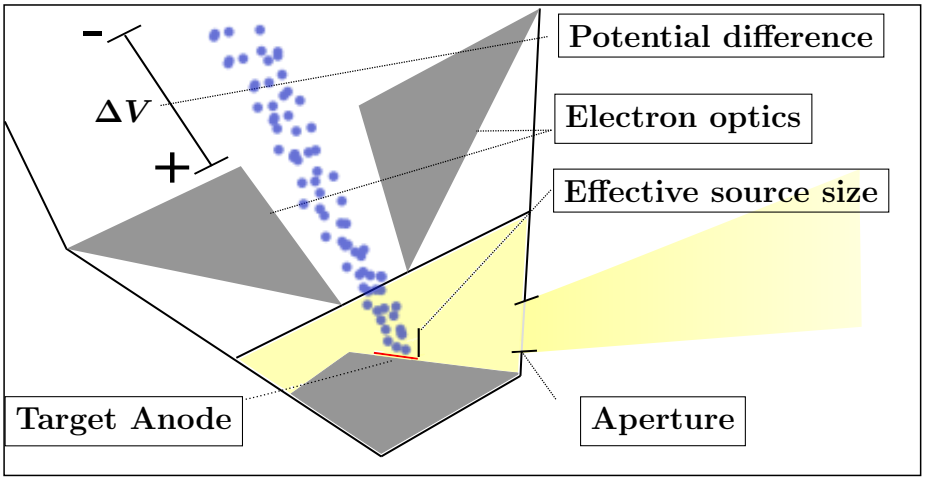

Figure 2.2: An illustration of the process of generating X-ray. The blue coloured circle represents electrons, accelerated by a potential difference and focused by electron optics towards the target anode, illustrated with red, generating X-ray, illustrated with yellow, as a product of the impact.

The process starts with a current passing through a filament to release electrons by thermionic emission. Accelerated by a potential difference, ΔV, and focused by a system of electron optics, the electron beam reaches the target anode with a kinetic energy

$$E_{max} = e\Delta V, \tag{2.2}$$

where $e = 1.6 \times 10^{-19}$ C. Most of the energy coming from the electron beam is transformed into heat while the remaining energy (at the scale of $\sim 1\%$) is converted into X-rays by two processes; Coulomb interactions and photoelectric excitation[17].

The first process is scattering caused by Coulomb interactions between the incoming electrons and the charge distribution of the target material. As the incoming electrons decelerate, they lose their kinetic energy in processes that span from single interactions to a cascade of interaction events with the target material, emitting a smooth continuous spectrum known as *bremsstrahlung* radiation. This process is modelled through Kramers' law, which states that the photon intensity

$$I(E) = KZ(E_{max} - E)E, \tag{2.3}$$

where Z is the atomic number, K is a constant, and E is the energy of the radiation[18]. The second process occurs if the incoming electron has enough energy to ionise a target material atom by photoelectric excitation of core-level electrons. The core hole is relaxed by a bound electron at higher energy, with the emission of photons with energies defined by the difference in binding energies between the bound states. The result is *characteristic radiation*, a set of discrete spectral lines characteristic to the target material. Fig. 2.3 shows an example of an X-ray spectrum from a Tungsten anode and how it changes as the acceleration voltage and the tube current change.

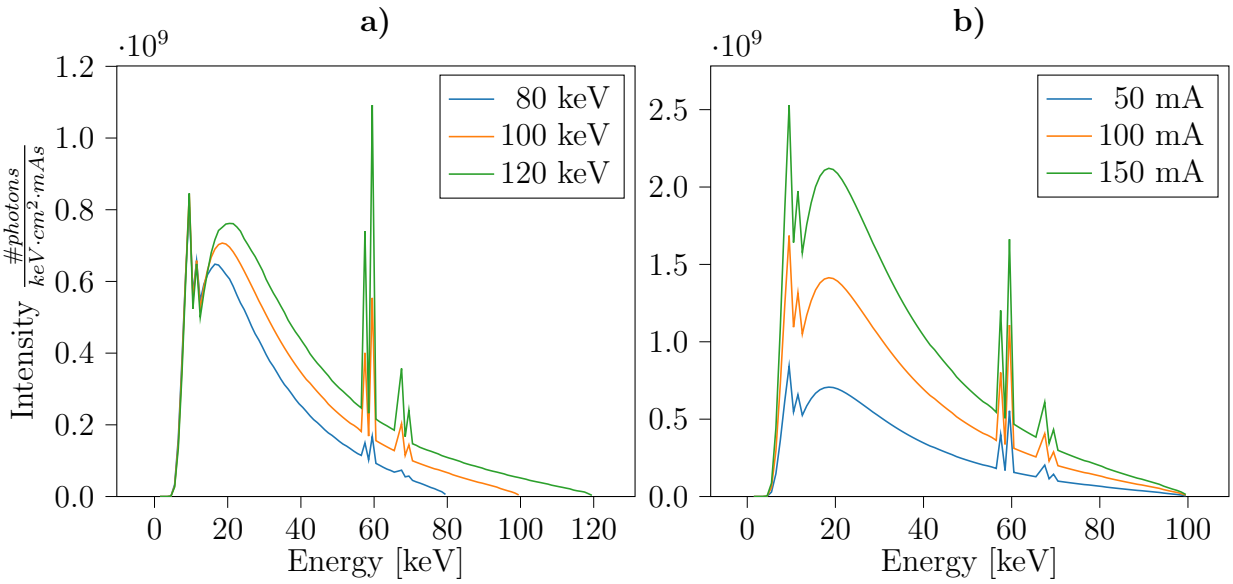

Figure 2.3: The two plots show numerical calculations of Tungsten's characteristic X-ray spectrum. **a)** shows how the spectrum changes as the acceleration voltage changes. **b)** shows how the spectrum changes as the tube current changes. The numerical tools are provided by Spekpy[19].

The area at which the electrons hit the target anode defines the source size and depends on the electron optics ability to focus the electron beam, increasing in difficulty with the beam power, defined as

$$P = I\Delta V, \tag{2.4}$$

where I is the current of the beam. From the source, X-rays radiate isotropically with a flux dependent on P. A fraction of the photons exit through an aperture defining the X-ray beam divergence, as shown in Fig. 2.2.

Finally, the spectral radiance of the source as a function of the energy, $L(E)$, can be defined as

$$L(E) = \frac{PE}{A\Omega hc}, \tag{2.5}$$

where P is the emitted power, A is the area of the aperture, Ω is the solid angle, $h = 6.6 \times 10^{-34}$ Js and $c = 3 \times 10^{8}$ m/s in vacuum[20].

2.3 Interaction between matter and radiation

While X-rays irradiate the test sample, the transmitted X-ray intensity is reduced according to the material attenuating properties, in general, described by the mass attenuation coefficient, μ/ρ, in units of cm^2/g, where μ is the linear attenuation coefficient and ρ is the mass density.

For the keV regime, the most predominant causes for attenuation are described by photoelectric absorption (pe), incoherent scattering (ico), and coherent scattering (co). The total attenuation coefficient in this regime is then given as

$$\mu(E) = \sum_i \left(\frac{\mu_{pe}(E) + \mu_{ico}(E) + \mu_{co}(E)}{\rho} \right)_i \rho_i \omega_i, \tag{2.6}$$

where the sum is taken over the different elements of the material, ω is the normalised weight fraction, and E is the energy of the incoming photons[21]. Fig. 2.4 shows how these effects contribute to the attenuation of Epoxy Resin. In addition, Fig. 2.5 exemplifies the difference in attenuation for solid, liquid and gas.

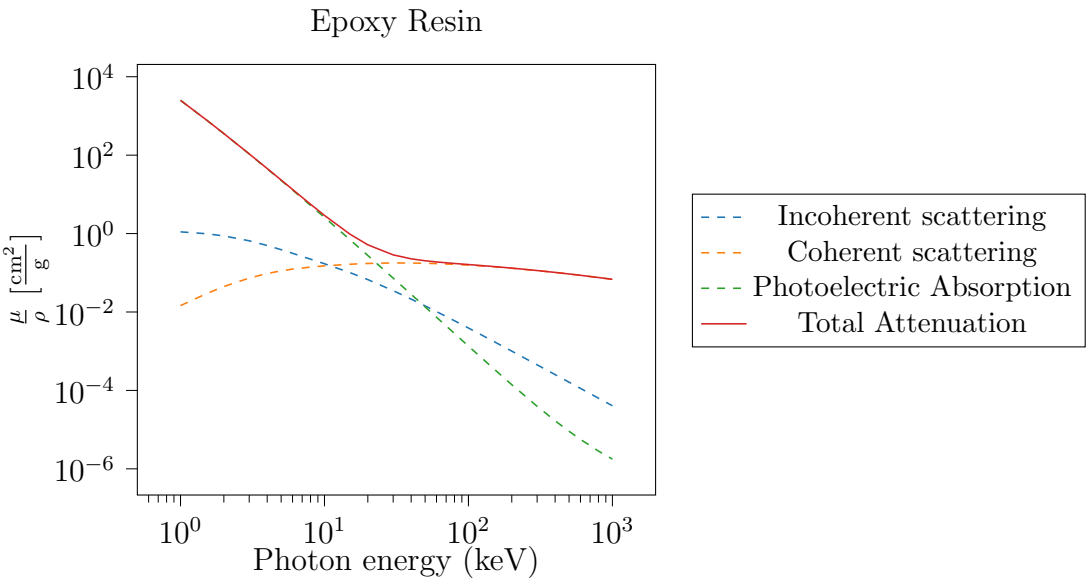

Figure 2.4: Numerical calculations of the mass attenuation coefficients of Epoxy Resin, $H_{24}C_{21}O_4$. The data is collected from NIST[22].

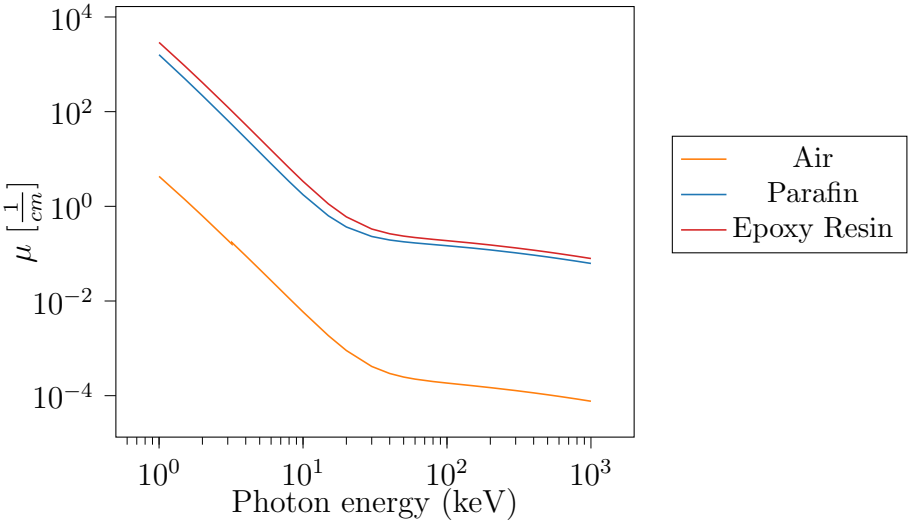

Figure 2.5: Numerical calculations of the linear attenuation coefficients for air, 78 % N_2 and 21 % O_2 and 1 % Ar with $\rho = 1.29\,\mathrm{g/cm^3}$, paraffin, $C_{15}H_{32}$ with $\rho = 0.85\,\mathrm{g/cm^3}$, and Epoxy Resin, $H_{24}C_{21}O_4$ with $\rho = 1.16\,\mathrm{g/cm^3}$. The data is collected from NIST[22].

Beer-Lambert law models the intensity changes from the attenuation and is derived by assuming that the intensity reduction along the X-ray path can be modelled as

$$\frac{dI}{dx} = -\mu(E)I(x), \tag{2.7}$$

where $I(x)$ is the X-ray intensity as a function of the distance x through the material, shown in Fig. 2.6. The general solution of Eq. 2.7 gives that the transmitted intensity

$$I_t(E, y, z) = I_0(E, y, z)e^{-x(y,z)\mu(E)}, \tag{2.8}$$

where I_0 is the intensity of the incoming X-ray beam, y and z give the path of the incident beam and $x(y, z)$ gives the distance through the material for that path. When the imaged object consists of different materials, liquids and gasses, it is necessary to consider that the attenuation constant varies along the path through the object. In that case, Eq 2.8 is modified and expressed as

$$I_t(E, y, z) = I_0(E, y, z)e^{-\int_0^{x(y,z)} \mu(E,y,z,x')dx'}. \tag{2.9}$$

Typically, the attenuation coefficient for gases is much smaller compared to that of liquids and solid materials, which can be observed in Fig. 2.5, and is therefore often approximated to zero. This is also why one ignores the air outside the sample in the calculations.

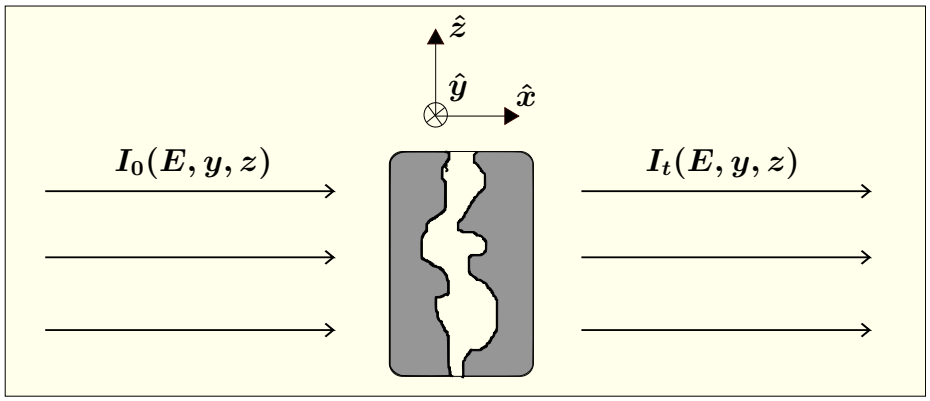

Figure 2.6: A schematic of the incoming and outgoing photons with a parallel beam geometry. The grey area represents solid material with a non-zero attenuation coefficient.

2.4 X-ray detectors

To detect the transmitted X-rays, a scintillator and a photodetector are used to convert the photons into an electrical signal. As the scintillator absorbs the X-rays, the internal material gets ionised or excited, causing long-wavelength radiation (visible light) emission. A photodetector, like a photomultiplier tube or a photodiode positioned behind the scintillator, captures this radiation and converts it into an electrical signal. Two factors determine the efficiency of these processes. The first is a pure geometrical scaling factor that reflects the X-ray intensity reduction per unit area that hits the detector. The second factor, called the intrinsic efficiency or the quantum detection efficiency, is described through Beer-Lambert law, Eq. 2.8, but now reflecting the absorbed rate as follows:

$$\epsilon_{int}(E) = 1 - e^{-\mu_s(E)t}, \tag{2.10}$$

where $\mu_s(E)$ and t describe the energy-dependent linear attenuation coefficient of the scintillator and its thickness, respectively[23]. As Eq. 2.10 indicates, selecting the appropriate material for the scintillator with a maximum attenuation peak around the most predominant energies of the X-ray spectrum will increase its efficiency. One commonly chosen material is caesium iodide[23].

By setting the detector in the yz-plane and the x-axis from the X-ray source to the detector, the equation for the measured intensity at a point (y, z) is given as

$$\begin{aligned} I_D(y,z) &= g \int_{E_{min}}^{E_{max}} \epsilon_{int}(E) I_t(E,y,z) dE \\ &= g \int_{E_{min}}^{E_{max}} I_0(E,y,z) \left(1 - e^{-\mu_s(E)t}\right) e^{-\int_0^{x(y,z)} \mu(E,y,z,x')dx'} dE, \end{aligned} \tag{2.11}$$

where the measured intensity is the integral over all energies in the spectrum, and g is a geometrical scaling factor assumed, for most CT setups, to be constant and equal for all points on the detector. Furthermore, for a non-quantitative CT, it is

not necessary to solve the integral in Eq. 2.11 since only the contrast is of interest. The X-ray spectrum is therefore treated as monochromatic, making the calculations more straightforward, but at the cost of lower contrast[24]. However, assuming that the materials and liquids in the radiated sample have a distinct attenuation, are homogeneous, and that any beam hardening effects can be neglected[1], the reduction in the contrast is negligible.

2.5 Tomography reconstruction

For each projection of the object, the intensity at a point (y, z) on the detector is given by Eq 2.11. Assuming a perfect detector with $\epsilon_{int} = 1$ for all relevant energies, and for simplicity, setting $g = 1$, the measured intensity can be expressed by Eq. 2.9. Assuming a monochromatic X-ray spectrum, the relevant term that describes the object is the exponent of Eq. 2.9. It is, therefore, convenient to define the projection function

$$p_\theta(s, z) = -ln\left(\frac{I_D}{I_0}\right) = \int \mu(s, t, z)dt, \tag{2.12}$$

where the coordinates (s, t) are defined such that t remains parallel to the X-rays (assuming a parallel beam geometry) as the system is rotated, while s remains parallel to the detector, as shown in Fig. 2.7.

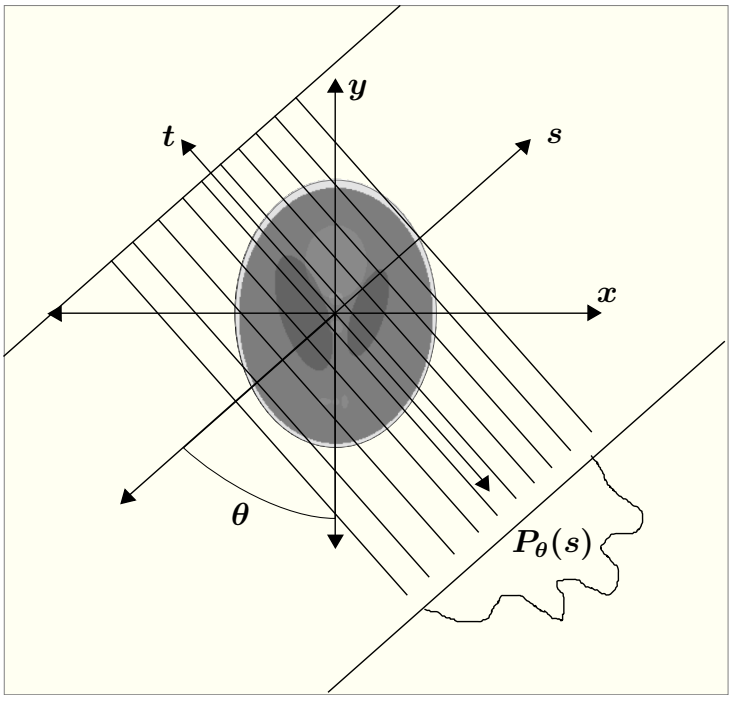

Figure 2.7: Illustrating Eq. 2.12 and how the orientation of the coordinate system is parameterised by s and t in relation to the xy-plane.

[1]Beam hardening refers to the phenomena where low-energy X-ray is absorbed at a higher rate than high-energy X-ray, causing the average energy of the spectrum to increase. The phenomenon is most prominent for high-density materials[25].

The central slice theorem states that it is mathematically feasible to achieve a perfect reconstruction of an object by applying a general projection function to the object, described by a general function f. For CT, the output of f would be the linear attenuation coefficients of the object. It states that for a fixed angle θ, the Fourier transform of Eq. 2.12 generates a slice in Fourier space with the same angle. By covering all angles, the entire Fourier space is mapped without any frequencies lost, implying no loss of information about the object either. Although the central slice theorem is independent of the beam geometries and dimensions, the core concept is more transparent through a proof in 2D (ignoring $\hat{z}$) that assumes a parallel beam geometry. Starting from the 1D Fourier transform of Eq. 2.12

$$\mathcal{F}[p_\theta(s)] = \int \left(\int \mu(s,t)dt \right) e^{-2\pi i k_s s} ds = P_\theta(k_s). \tag{2.13}$$

Followed by taking the 2D Fourier transform of the linear attenuation coefficient

$$\mathcal{F}[\mu(s,t)] = \int \int \mu(s,t) e^{-2\pi i k_s s} e^{-2\pi i k_t t} ds dt = \mu(k_s, k_t). \tag{2.14}$$

Setting $k_t = 0$, Eq. 2.13 reveals itself as

$$\int \left(\int \mu(s,t)dt \right) e^{-2\pi i k_s s} ds = \mathcal{F}[p_\theta(s)] = P_\theta(k_s). \tag{2.15}$$

Proving that for each projection acquired at the angle θ, one line rotated with angle θ is mapped in the Fourier domain, as shown in Fig. 2.8, proving the central slice theorem.

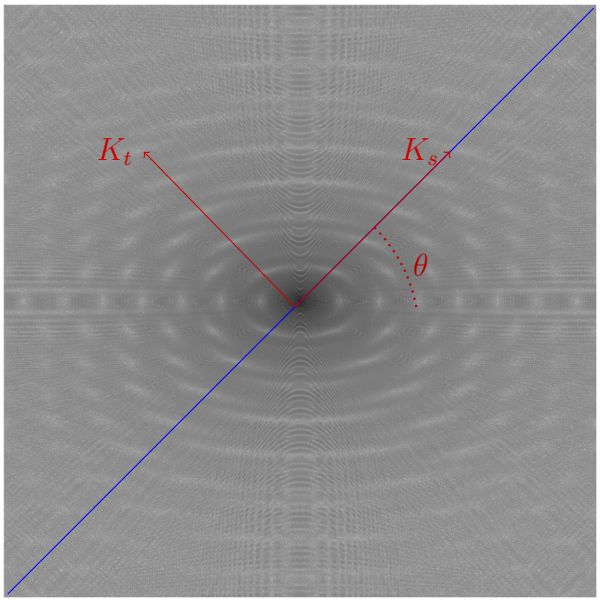

Figure 2.8: Illustrating the line in Fourier space mapped from a projection at angle θ. The image is the logarithm of the Fourier transform of the Shepp-Logan phantom[26].

In practice, the number of projections is discrete, and so is the pixel array of the detector, giving a lower bound to the resolution and introducing a sampling problem for higher frequencies as these are sampled less densely than lower frequencies. This becomes clear in Fig. 2.8 by adding several lines at different angles. Filtered back projection is a technique that compensates for this effect but is best understood by first looking at a simple back projection.

A simple back projection is performed by taking the value measured at a point on the detector, hence the solution to Eq. 2.11, and applying that value to all voxels[2] on the straight path between the source and that point. Repeating the process for several angles causes the values to add up, approximating the imaged object. Fig. 2.9 illustrates the idea of back projection and how the objects become apparent. It should be noted that the beam geometry introduces symmetry to the back projection method, dispensing the need for using all projection angles[27].

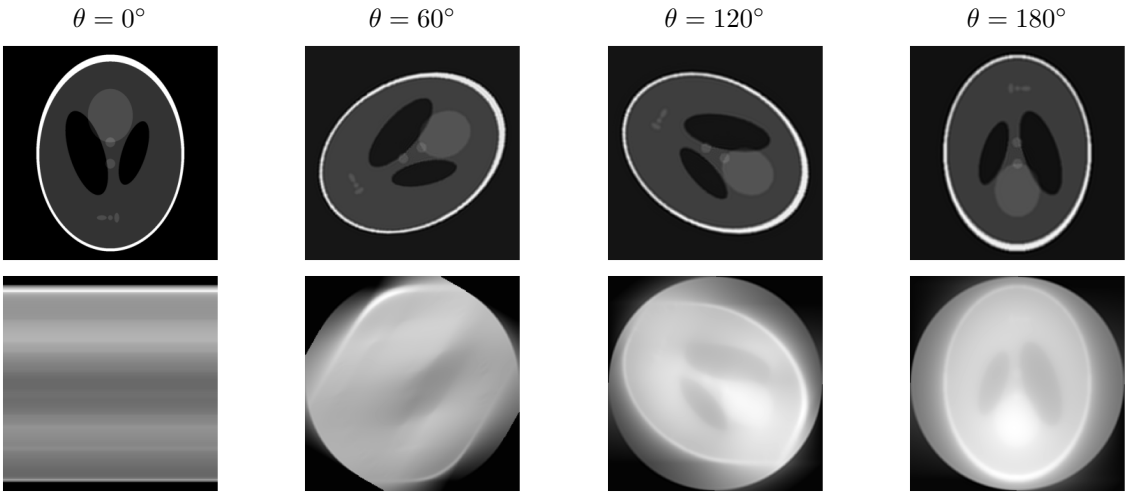

Figure 2.9: Illustrating the method of back projection using a Shepp-Logan phantom[26]. The first row illustrates the orientation of the phantom at angle θ, and the second row is the result of the back projection up to that angle. For this example, a projection is taken at every 0.5°.

As predicted from the central slice theorem and visible in the resulting image in Fig. 2.9, the higher frequencies of the image are sampled less dense than the lower ones, causing a blur of the image. The filtered back projection method compensates for this effect by applying a filter that suppresses the lower frequencies and enhances the higher frequencies.

There are several ways to do this, but perhaps the simplest way is to multiply the filter with the back-projected image in Fourier space. Since the blurring has a $1/f$ dependency, f denoting the frequency, a simple but effective filter known in the literature as a ramp filter could be applied. In the frequency domain it is defined as

$$H_R = (k_x^2 + k_y^2)^{\frac{1}{2}}, \tag{2.16}$$

where k_y and k_x are the spatial frequencies. A low-pass filter is also always added to avoid amplifying high-frequency noise[28]. The effect of the ramp filter is shown

[2] A voxel is defined as a volumetric pixel.

in Fig. 2.10. Several other filters also exist, and for additional study, chapter 2 of "Industrial X-ray computed tomography" is recommended[15].

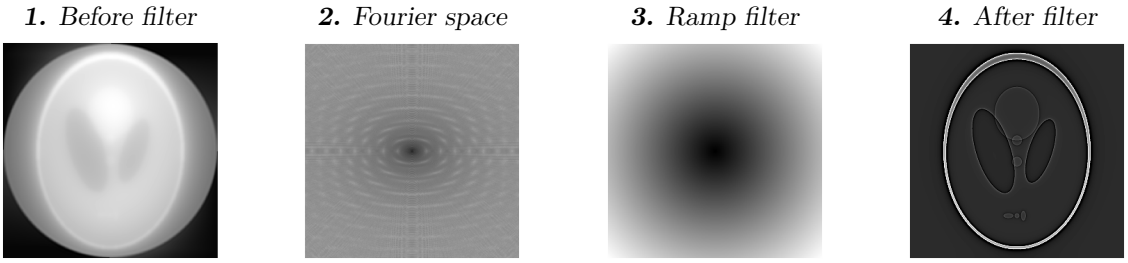

Figure 2.10: Illustrating the process of applying a ramp filter in Fourier space. Image 1 is the result from the back projection shown in Fig. 2.9. Image 2 is the Fourier transform of image 1 in a logarithmic scale for illustrative purposes. Image 3 shows a ramp filter in 2d space, and image 4 is the result of multiplying image 2 and image 3 together and taking the inverse Fourier transform. The contrast in image 1 and 4 has been adjusted for illustrative purposes.

2.6 Resolution and imaging effects

The final image spatial resolution depends on the quality of each projection, and some of the parameters that affect this quality can be highlighted through a geometrical consideration. Naturally, these effects depend on the beam geometry, and a cone beam geometry will therefore be assumed.

The finite size of the source causes a blurring, as illustrated in Fig. 2.11, and is referred to as the geometrical unsharpness, U_g, which through a trigonometric evaluation, can be expressed as

$$U_g = a\frac{d_2}{d_1} = a(m-1), \tag{2.17}$$

where a is the effective source size, d_1 and d_2 is the distance from source to object and object to detector and m is given by Eq. 2.1. This is also known as the penumbra effect[29].

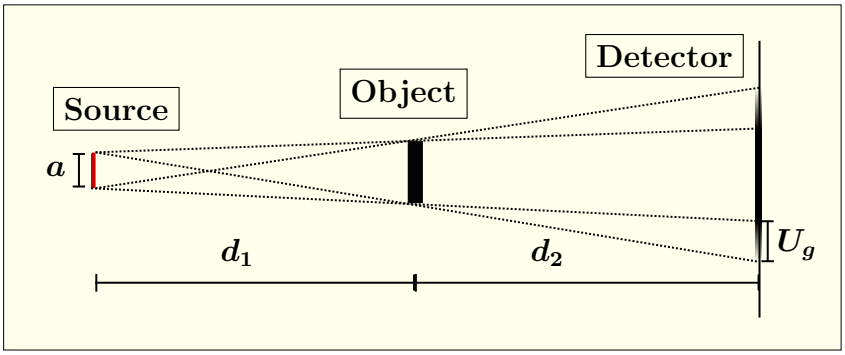

Figure 2.11: Illustrating the unsharpness effect caused by a source size greater than zero.

Due to the detector, some additional unsharpness, U_d, is included, and the total unsharpness can be expressed as

$$U = \sqrt{U_g^2 + U_d^2}. \tag{2.18}$$

The detector's unsharpness can come from several reasons, such as misalignment of the detector relative to the imaged object and the source, or cross-talk[3] in the scintillator[30,31]. The value of U_d is easiest found from detector calibration[32].

To get the complete picture of the spatial resolution, one also has to consider the pixel size that arises from the discrete nature of the detector, hence the detector matrix size. The obtained pixel size of each image is determined by the image size on the detector and the matrix size as follows

$$pixel\ size = \frac{Image\ size}{Matrix\ size} := \Delta x. \tag{2.19}$$

This also limits the smallest object that can be detected, as the image of the object on the detector should at least be in the magnitude of 2 pixels by the Nyquist-Shannon sampling theorem[33]. This does not include unsharpness, and from its definition, it is clear that the effective source size also sets a lower bound for the resolution.

As discussed in chapter 2.5, the central slice theorem states that each projection represents a line in Fourier space where the angle between the projections are equivalent to the angle between these lines. From a geometrical evaluation, one can derive the maximum azimuth frequency length between two projections as shown in Fig. 2.12. If the total number of projections is N_p, then the angle between the projections is given as

$$\Delta\phi = \frac{\pi}{N_p}, \tag{2.20}$$

assuming that each projection is taken with a constant angular step. Further, a trigonometric evaluation of Fig. 2.12 gives that the maximum azimuth frequency length

$$\Delta k_\phi = k^{max}\Delta\phi, \tag{2.21}$$

where the maximum measured frequency k^{max}, hence the Nyquist frequency, is related to the pixel size as follows

$$k^{max} = \frac{1}{2\Delta x}. \tag{2.22}$$

Combining Eq. 2.20 and Eq. 2.22 with Eq. 2.21 one get that

$$\Delta k_\phi = \frac{1}{2\Delta x}\frac{\pi}{N_p}. \tag{2.23}$$

The limiting point where the maximum azimuth frequency length exceeds the radial frequency length, hence $\Delta k_\phi = \Delta k_r$, can be derived by noting that

$$\Delta k_r = \frac{2k^{max}}{N_r} = \frac{1}{\Delta x N_r}, \tag{2.24}$$

[3]Cross-talk is an effect caused by signals from neighbouring pixels in the detector affecting each other.

where N_r is the number of frequencies measured per projection. Combined with Eq. 2.23, this gives

$$N_p = \frac{\pi}{2} N_r. \tag{2.25}$$

When the number of projections is less than this, the resolution of the final reconstructed image will be limited by the lack of projections.

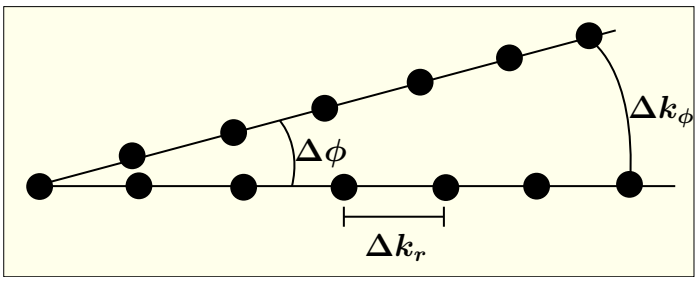

Figure 2.12: Illustrating discrete samples of frequencies in Fourier space gather from two projections at different angles.

2.7 Image processing

The resulting image after the reconstruction will be a map of values reflecting the attenuation coefficients of the imaged object, meaning that a simple threshold method could be applied to label the different materials as long as their values are sufficiently distinguishable. To decide the threshold value/values, one has several options. Otsu demonstrated one such method that focused on maximising the separability between the label classes by analysing the greyscale histogram of the image[34]. Regardless of the thresholding method, it will always be vulnerable to noise in the image. For this reason, some filtering is usually required. Two common filters that may serve this purpose are the median filter and the non-local means filter, both meant to handle random noise in the image.

The median filter relies on a simple median algorithm that updates a voxel value based on the median intensity of its neighbourhood. One such neighbourhood is defined by its size and shape, where the central value is to be updated. A simple 2D example is a $3x3$ square neighbourhood such as the following

$$\begin{bmatrix} 1 & 2 & 2 \\ 1 & 3 & 4 \\ 2 & 3 & 4 \end{bmatrix} \xrightarrow{\text{median filter}} \begin{bmatrix} 1 & 2 & 2 \\ 1 & \mathbf{2} & 4 \\ 2 & 3 & 4 \end{bmatrix}$$

The central value would then be updated to the median of all values within that neighbourhood, which for this case was 2. After iterating through all voxels of the image, with some adjustments to the algorithm for the image boundaries, the new values are updated. Repeating the procedure would blur away more noise but at the cost of blurring the image as a whole. Such a filter deals with noise surrounded by true values effectively. However, it results in a blurring of edges and can, for extremely noisy areas, enhance it[35].

The Non-Local means, NLM, filter is a far more sophisticated filter that updates a voxel value based on the mean of similar non-local neighbourhoods. From the paper "A non-local algorithm for image denoising"[36], the NLM method is described as follows: Let v be a representation of a noisy image defined as

$$v = \{v(i)|i \in I\}, \tag{2.26}$$

where i represents a voxel from the image I. The NLM filter gives a new representation of the image

$$NL[v](i) = \sum_{j \in I} w(i,j)v(j), \tag{2.27}$$

where the weight $w(i,j)$ is a value between 1 and 0, that satisfy $\sum_j w(i,j) = 1$, and represents the similarity between the neighbourhoods, $\mathcal{N}_i$, of two voxels, measured by their intensities $v(\mathcal{N}_i)$. Each voxel is therefore updated as a weighted average between all voxels in the image. The neighbourhoods are defined by size and shape, commonly cubic or spherical, with the voxel of interest in the centre, and the similarity between two neighbourhoods is measured with the Gaussian-weighted Euclidean distance

$$||v(\mathcal{N}_i) - v(\mathcal{N}_j)||^2_{2,a}. \tag{2.28}$$

where a is the standard deviation of the Gaussian kernel, referred to as the intensity standard deviation. The final expression for the weight function is then expressed as

$$w(i,j) = \frac{1}{C(i)} e^{-\frac{||v(\mathcal{N}_i) - v(\mathcal{N}_j)||^2_{2,a}}{h^2}}, \tag{2.29}$$

where h is referred to as the spatial standard deviation for the weights, and $C(i)$ acts as a normalisation constant defined as

$$C(i) = \sum_i e^{-\frac{||v(\mathcal{N}_i) - v(\mathcal{N}_j)||^2_{2,a}}{h^2}}. \tag{2.30}$$

As seen from the mathematics, the filter is adequate for reducing noise while preserving the textures in the image. On the other hand, it is much more computationally demanding than, say, the median filter. A method to reduce the computation time is to reduce the search window for the neighbours, often defined as a ball with a given radius around the voxel, which is to be updated.

Chapter 3

Method

3.1 Preparation of test object

A suitable test sample was constructed by extracting a connected sub-pore system from a digitalised sandstone and embedding it in a 0.7 mm diameter cylinder with a height of 0.9 mm, aligning the pore space as close as possible to the cylinder's centre of rotation. The cylinder and the pore system were then scaled up asymmetrically to a final diameter of 4.36 mm and a height of 9.77 mm before it was produced by 3D printing.

To facilitate the injection of liquids into the pore system, a funnel was added at the end of the cylinder, shown in Fig. 3.1a. As the smallest opening in the pore system was measured at 106 µm, a 22 µm resolution UV-based 3D-printer was employed to avoid any pores from closing and, in general, preserve the details of the pore structure[37]. The 3D printer, a "Phrozen sonic mini 8k", used "Aqua-Gray 8k" as material, which is a type of Epoxy Resin provided by Phrozen[37,38]. An image segmented 3D scan of the final sample and images of the sample are shown in Fig 3.1.

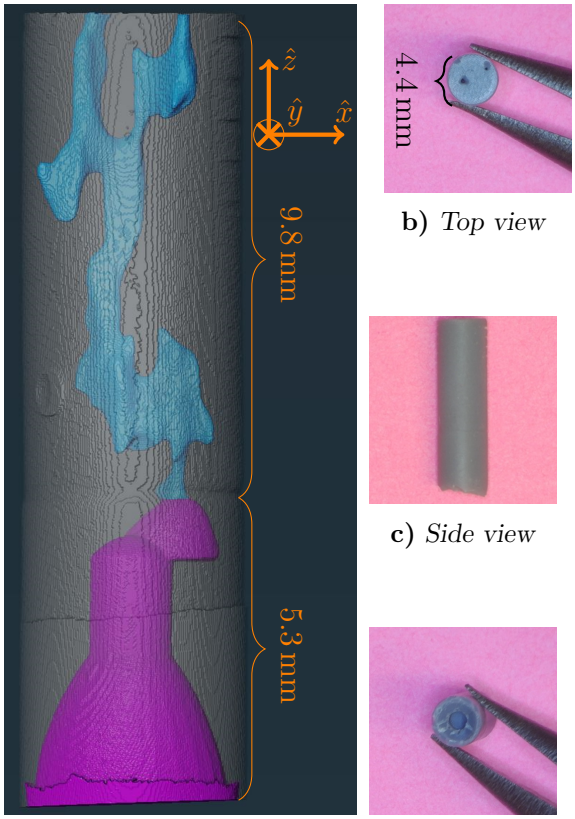

a) *Innside* **b)** *Top view* **c)** *Side view* **d)** *Bot view*

Figure 3.1: Image **a)** shows a segmented reconstructed CT scan of the sample processed and visually shown in AVIZO[39]. The pore system is labelled with blue, the funnel in purple, and the cylinder embedding the system in transparent grey. Images **b)** to **d)** shows the sample from different angles.

3.2 Pump

To control the flow of liquids inside the test sample, it was necessary to design a pump compact enough to fit the rotating stage of the CT scanner and for it to be wirelessly controllable to avoid any cable entanglements. In addition, it had to be capable of pumping at a rate of microliter per minute.

The core components of the pump are depicted in Fig. 3.2. Through Bluetooth, an Arduino MKR 1010 wifi[40] is set to output a voltage at a user-specified frequency, f. The output frequency controls a micro stepper which again controls a stepper motor. Combining the two gave a step length of 0.0072° degrees, taking one step per pulse. As the stepper motor rotates, a system composed of a gear and a screw translates the rotational motion into the linear motion of a syringe plunger, pushing the liquids inside the syringe barrel through a tubing system and out through the sample holder. By using a 100 µL Hamilton syringe with length 60 mm, the final pump rate can be calculated as $f/2000$ µm/min. A rough estimate, assuming that five discrete steps per second can be approximated as continuous, would then give that the pump is capable of producing 2.5 nL/min in a smooth manner. The pump is also equally capable of aspirating liquids at the same level as producing, which the user could control through the Arduino during the experiment.

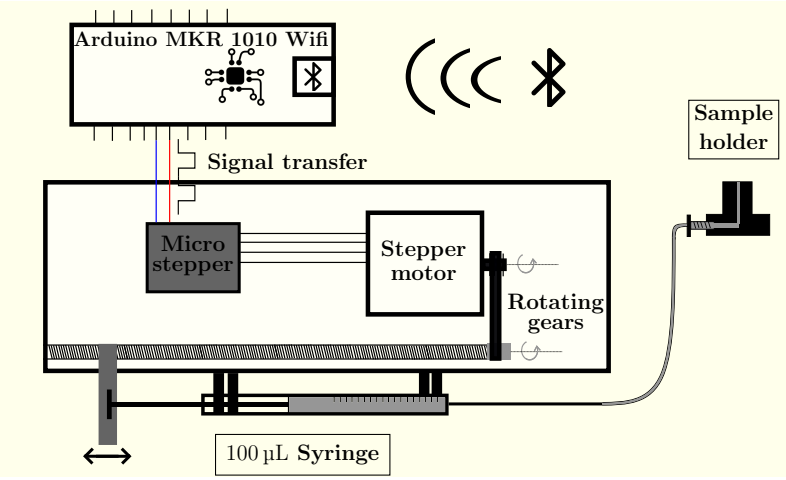

Figure 3.2: The Arduino MKR 1010 Wifi receives and interprets a Bluetooth signal which then outputs a fixed voltage at a given frequency. Through a system consisting of a micro stepper, a stepper motor, a gear and a screw the frequency of the signal controls the pushing rate of a plunder of a syringe. The fluid inside the syringe is then pushed through a tubing system at which the sample is placed at the very end.

3.3 Experimental setup

To prepare for the experiment, the test sample was placed inside a protective sleeve and positioned onto the sample holder. The purpose of the sleeve was to ensure that all the liquids from the sample holder were directed through the funnel and into the pore system, as any leakage would be suboptimal. The sample holder was then connected to the pump attached to the rotating stage of the CT scanner. Finally, on top of the stage, the sample holder was placed onto an X-Y positioning table to co-align the rotational axis of the stage and the pore system to reduce reconstruction errors that occur as a function of radial distance from the rotation axis[1]. An Image of the setup is shown in Fig. 3.3.

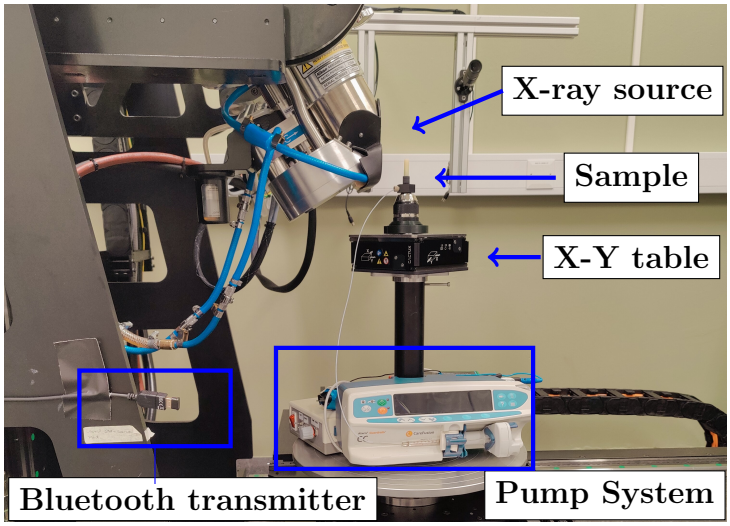

Figure 3.3: The experimental setup, which also includes a detector not shown in the frame of this image.

For the experiment, a custom-built Nikon system with a NIKON C1 Compact Precision 5 Axis CT scanner, a rotating target and a Perkin Elmer 1621 EHS flat panel detector was utilised to require a sequence of 57 repeating CT scans while paraffin was drained from the pore system[41]. Table 3.1 shows the scanning parameters used throughout the experiment. Each scan was acquired during 40 seconds, followed by a 20-second resetting time before the next scan commenced, meaning that the resulting image from each scan represented the average state of the system within the 40-second scanning window. In addition, a ground truth scan was conducted of the sample without any liquids inside the system. The same parameters as in Table 3.1 were used for this scan but with 720 projections instead.

Table 3.1: Parameters for the CT scan acquisition taken during the experiment.

# Projections	80
Acceleration voltage	115 keV
Power	24.9 W
Exposure time	500 ms
Gain	24 dB
Voxel size	5.68 µm

Two measures were taken to prevent air bubbles from mixing with liquid, causing unpredictable fluid movement during the experiment. The first was to use Exxsol D-60, paraffin, as the wetting fluid, a viscous liquid that matches the oil-based characteristics of the Epoxy Resin material[42]. The second measure was to pump the liquid inside the pore system with a relatively high pumping rate right before the experiment, pushing air bubbles trapped inside cavities out of the system. When a clear paraffin-air interface was at the desired position inside the pores, the paraffin was extracted from the bottom of the sample holder at a low rate. In practice, the pump suffered from imperfections resulting in a small unknown leak at the nanoliter scale located before the sample holder. To compensate for this leak, the pump was set to constantly inject 10 nL/min of paraffin, giving a net result of paraffin being drained from the pore system and a net movement of the fluid interface in the negative z-direction during the image acquisition.

3.4 Reconstruction and filtering

The reconstruction software, "CT pro-3D", provided by Nikon, was used for the tomographic reconstructions[43]. All scans were sent through the same reconstruction and filtering pipeline involving a standard filtered back projection method using a ramp filter provided by the reconstruction software. Additionally, a median filter and a non-local mean filter, both provided by AVIZO, were applied[39]. The filter parameters are shown in Table 3.2 and are explained in depth in section 2.7.

As all of the filtered tomograms were to be compared to each other, it was necessary to ensure they were aligned correctly. A small metal piece located on the sample outside the area of interest was used for this. Exploiting its highly attenuating properties, which made it simple to localise. This approach was preferred over

relying on the orientation angles provided by the Nikon Scanner since they were found to be unreliable.

Table 3.2: Filter parameters used on all reconstructed images.

Median filter	
Neighbourhood size	7x7x7 voxels
Neighbourhood shape	Cubic
Non-Local Means filter	
Intensity standard deviation	5
Spatial standard deviation	0.2
Search window	10 voxels
Neighbourhood shape	Spherical
Neighbourhood radius	3 voxels

Post filtration, the matrix was separated from the pore space in the ground truth using the thresholding method described in section 2.7. After an alignment with the rest of the filtered images, the ground truth was applied as a mask, excluding data outside the pore space.

3.5 Grey value analysis

After filtering and masking each tomogram, one is left with a set of 3D images where each voxel value of the image represents the average attenuation of that voxel throughout the 40-second imaging time. One can expect a significant contrast difference between the paraffin and the air, as exemplified in Fig. 2.5. Therefore, to get a rough estimate of the shape and location of the fluid interface in each image, an calculation of the average grey value inside the pore system was performed for each cross-section of the system. Each average grey value would then give an estimate of the ratio of paraffin to air for each cross-section.

3.6 Fluid interface analysis

For a more thorough analysis of how the system developed over time, it was necessary to label the fluid interface. First, the thresholding method, as described in section 2.7, was employed to label the two different fluids within the system. To get the fluid interface within the pore system, one only included the voxels at the boundary between the two labels, giving a data set representing the fluid interface.

To analyse the temporal development of the fluid interface, well-defined mathematical surfaces were fitted to the area of interest using a non-linear least square regression method provided by Scipy[44,45]. Using these surfaces, two methods were utilised to trace the temporal development of the fluid interface.

The first method, the curvature method, focuses on parabolic surfaces. As illustrated in Fig. 3.4, the method uses the centroid of the sphere tangential to the minima of the paraboloid with the same curvature as calculated for that minima. From the centroid, a grid of tracing points, separated by a constant angle, is chosen on the parabola, which is then assumed to grow radially from the centroid onto the next parabola representing the next time step. The curvature value of a point on a 3D surface was calculated using the mean curvature[46].

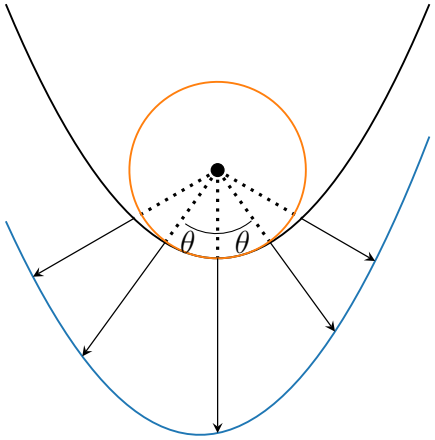

Figure 3.4: Illustrating the curvature method to trace the displacements of one parabola to the next.

The second method is more straightforward as it only analyses the displacements of a grid of tracing points on the fitted surfaces along one direction. A method best suited when the surfaces are complex and or when the changes are dominant in one direction. Fig. 3.5 illustrates the method, named the one-directional method.

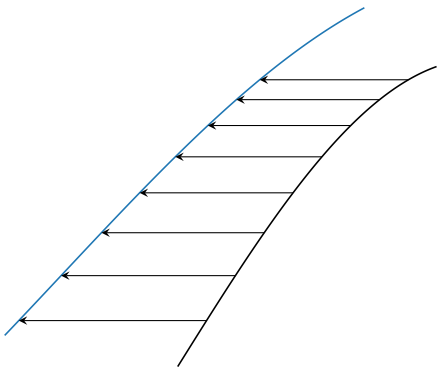

Figure 3.5: Illustrating the one-directional method to trace the displacements of a surface onto the next.

3.7 Evaluation of the fitted surfaces

The value of fitting surfaces to the fluid interface areas is to suppress the effect of noise. Unfortunately, it will also suppress anomaly features of the fluid interface that are not captured by the assumed surface morphology and cannot be attributed to noise. An analysis of the fluid interface compared to the fitted surfaces is therefore performed by calculating the residual distance from the fluid interface points onto the fitted surface. A standard deviation from the residual distribution can then be calculated, and by isolating outliers defined as all fluid interface points with a residual larger the three times the standard deviation, σ, one would expect from a Gaussian random distribution that the fraction of outliers is 0.3%. Any deviations from this could indicate that the assumed geometry of the fitted surfaces is oversimplified, Fig. 3.6 illustrates this.

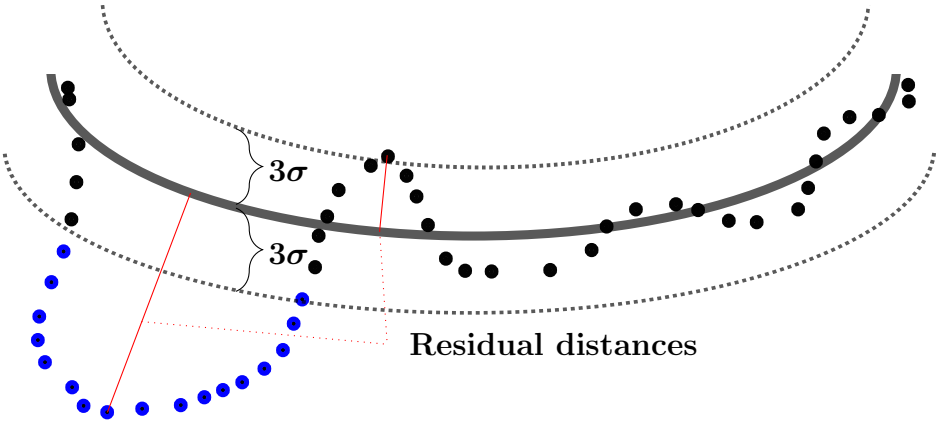

Figure 3.6: Illustrating the fluid interface points with a fitted surface to these points and the process of isolating any fluid interface points exceeding a distance to the surface equal to 3 times the standard deviation of the residual distances.

Chapter 4

Results

The most relevant part of the pore structure at which the fluid interface was maintained throughout the experiment is shown in Fig. 4.1. Paraffin escaped the system from below, causing air to enter the system from above, creating a net velocity of the fluid interface in the $-\hat{z}$ direction. Both the velocity and the morphology of the paraffin-air interface are expected to be affected by the cross-sectional areas, orthogonal to the height z, of the pore space. The cross-sectional area as a function of z is therefore mapped and displayed in Fig. 4.1c (with the height relative to the bottom of the pore system). As seen from Fig. 4.1c, the smallest cross-sectional area of the pore space is measured $0.13\,\mathrm{mm}^2$ and the largest measured $0.39\,\mathrm{mm}^2$, with an average area of $0.24\,\mathrm{mm}^2$. These measurements are extracted from the high-resolution ground truth scan.

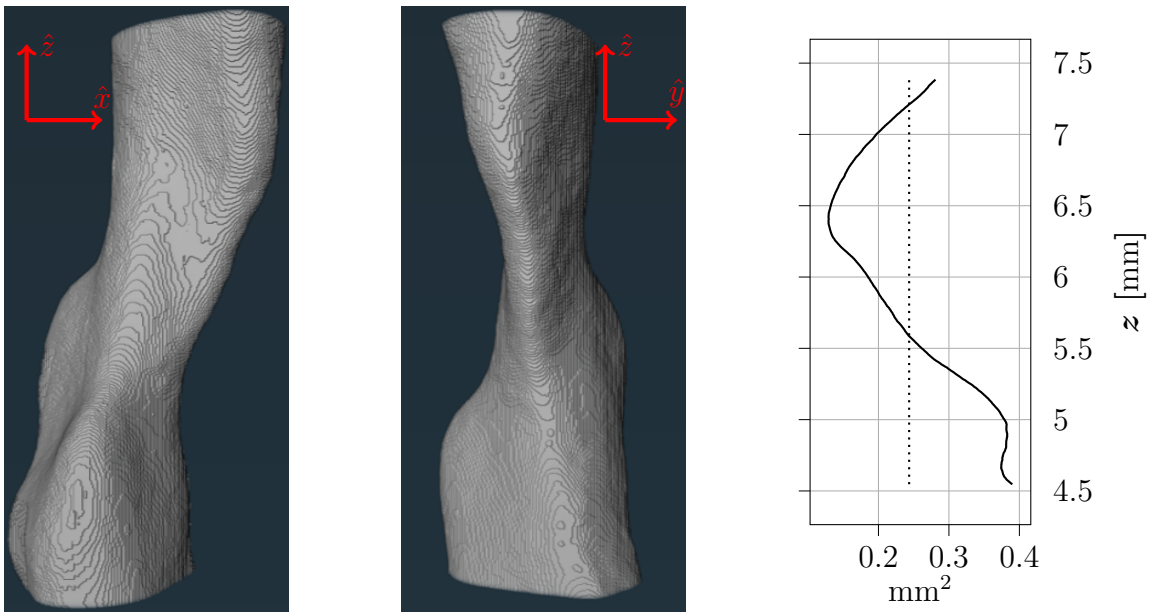

a) *xz-plane* **b)** *yz-plane* **c)** *Cross-sectional pore area*

Figure 4.1: **a)** and **b)** shows a graphical representation of the most relevant part of the pore system for this analysis, with a defined coordinate system. **c)** shows the pore cross-sectional area as a function of the height z, with the average area marked with a dotted line.

Throughout the experiment, a total of 57 CT scans were taken at 1-minute intervals. To simplify the notation when referring to these scans, they will be denoted as time steps, T_n, where n represents a number from 0 to 56. This notation allows us to associate each scan with the scan number and the corresponding minute at which it was acquired.

During the experiment, paraffin exhibited retrograded motion along the pore walls, resulting in areas behind the displacement front being re-filled with paraffin. This observation is clearly depicted in Fig. 4.2, showing the system's states at T_0, T_{30}, and T_{41}. Consequently, it becomes necessary to define the specific areas for further analysis. These areas include the lowest part of the fluid interface, named the displacement front, denoted by red squares in Fig. 4.2, and the region marked with blue squares in Fig. 4.2. The appearance of this region occurs at T_{27} as a result of paraffin gradually filling the volume pushing the interface with air away from the pore wall. This area will be referred to as the interface area along the pore wall, hereafter, IPW-area for short.

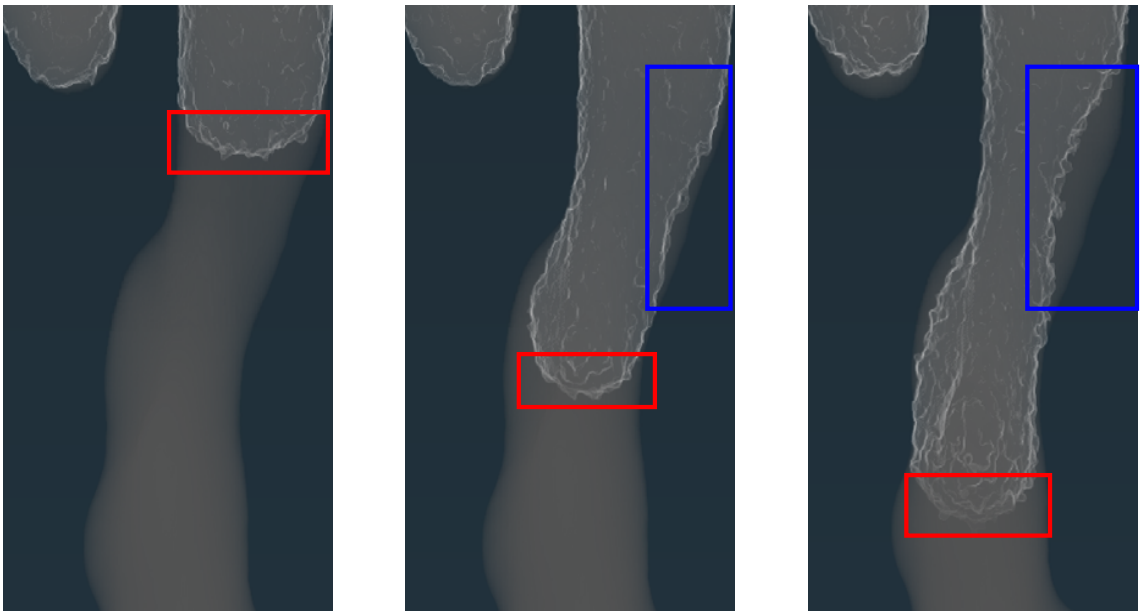

a) *System state at* T_0 **b)** *System state at* T_{30} **c)** *System state at* T_{41}

Figure 4.2: Voxel rendering of the system, at T_0, T_{30} and T_{41}, showing the paraffin-air interface (air is coming in from the top labelled with light grey colouring). The red rectangles indicate the displacement front of the fluid interface, and the blue square indicates the IPW-area of the fluid interface.

A clear definition of the fluid interface area belonging to the displacement front is necessary to be able to fit any mathematical surface. If it were not for the retrograde motion of paraffin, defining this area would be a straightforward task, as it would simply be the fluid interface, bound by the contact points with the pore wall, as would be the case in Fig. 4.2a and Fig. 4.2c. Instead, due to situations where there is no clear boundary between the pore wall and the fluid interface that could constrain the displacement front, as would be the case in Fig. 4.2b, the grey value analysis was employed to establish an upper boundary in z to the displacement fronts considering all fluid interface voxels with $z < z_{lim}$ as part of the displacement

front.

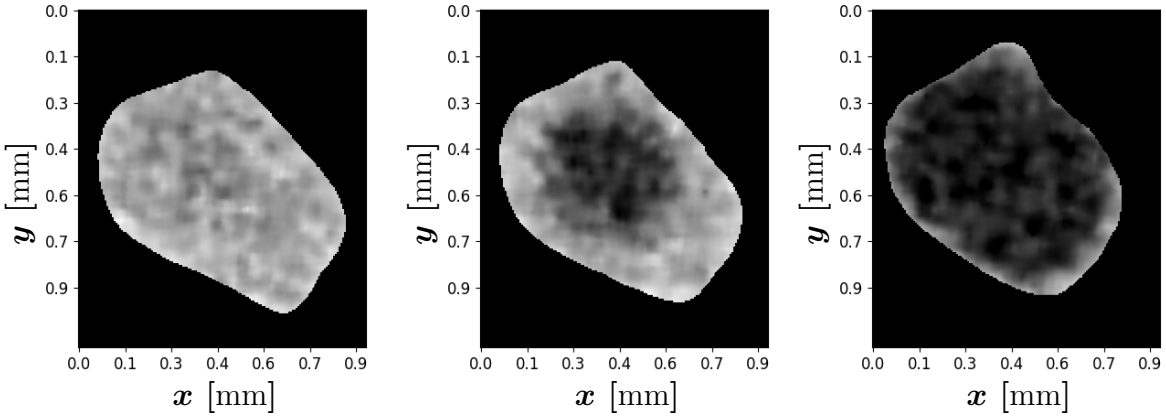

a) z=4.58 mm **b)** z=4.66 mm **c)** z=4.89 mm

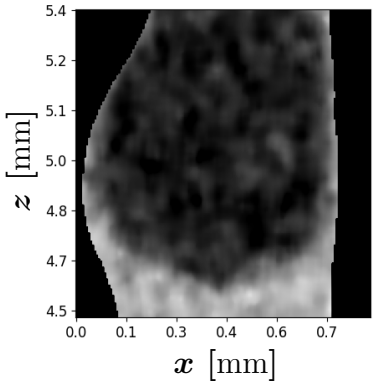

d) *Cross-section in the xy-plane*

Figure 4.3: Image **a)** to **c)** shows three different cross-sections of the resulting filtered tomogram at T_{52}, while **d)** shows a cross-section in the xy-plane also for T_{52}. The grey values of the images are darkest for air and brightest for paraffin, and absolute black indicates the pore matrix.

The grey value analysis revealed a distinct contrast between paraffin and air, as shown in Fig. 4.3, and by the results of the average grey value analysis shown in Fig. 4.4 for T_5, T_{15} and T_{25}. To provide a more rigorous description of the average grey values, sigmoid curves were utilised, defined as

$$S(z) = \frac{a_0}{1 + e^{-a_1(z-a_2)}} + a_3, \tag{4.1}$$

where the coefficients a_n are fitted by a non-linear least square regression method to the average grey value of the cross-sections along the z. As one progresses upwards in the system, the average grey values tend to stagnate, indicating a constant ratio between air and paraffin for each cross-section. To optimise the fitting of the sigmoid curves, the analysis was stopped after such a stagnation to avoid the influence from areas, such as the IPW-area, found further up in the system.

Based on the sigmoid curves, the upper limit used to define the displacement front was determined as the z-value with the maximum curvature in the lower portions of the sigmoid curves, as illustrated in Fig. 4.4.

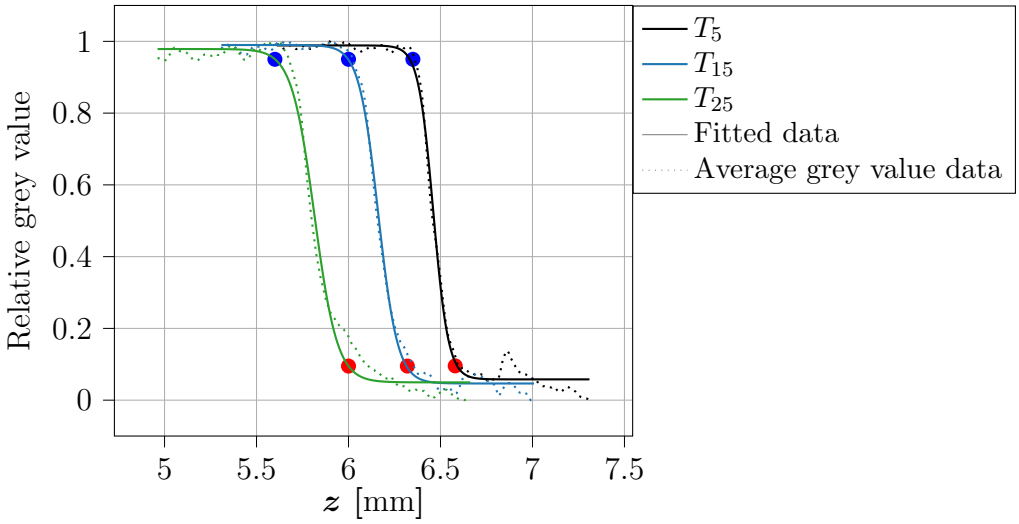

Figure 4.4: The normalised average grey value for each cross-section along the z-axis of the pore system is shown with a dotted line for T_5, T_{15} and T_{25}. The fitted sigmoid curves for this data are shown with a continuous line. In addition, points with the highest curvature for the lower part and the upper part of the sigmoid curve are represented with red and blue dots, respectively.

To further describe the displacement front, a 4th-degree polynomial surface was fitted to its interface voxels. This choice of surface was made to resemble the apparent parabolic shape of the displacement front while allowing for less enforced symmetry compared to a standard parabolic surface. As an illustration of the outcome, the fitted surface to the displacement front at T_0 is displayed in Fig. 4.5a.

The IPW-area is defined as the fluid interface within the region marked by the blue square in Fig. 4.2, naturally bounded by the contact points with the pore wall. A hyperbolic paraboloid was fitted to its interface voxels to characterise its evolution. Fig. 4.5b provides an example of such a fit.

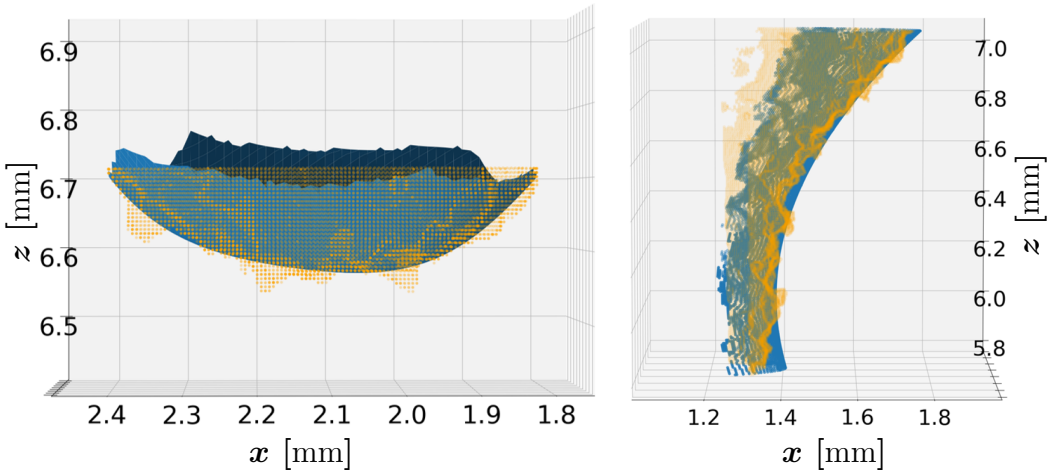

a) *Displacement front* **b)** *IPW-area*

Figure 4.5: The fluid interface voxels for the displacement front, **a)**, and the IPW-area, **b)**, are illustrated with orange scatter points, while the corresponding fitted surfaces are illustrated in blue.

To assess how well the sigmoid curves and the surfaces were fitted to the corresponding data points, the R^2-score was utilised. The results are presented in Fig. 4.6, demonstrating a good fit for all fitted surfaces. Moreover, to assess the stability of each curve fit, multiple initial conditions were tested for each fitted surface when the non-linear least square regression method was used, with negligible differences in the result. This provides further confirmation of the accuracy and reliability of the fitting process. While the fitting quality was generally good for all surfaces, it is notable that the fitting quality improved significantly after the 30-minute time mark for the displacement front.

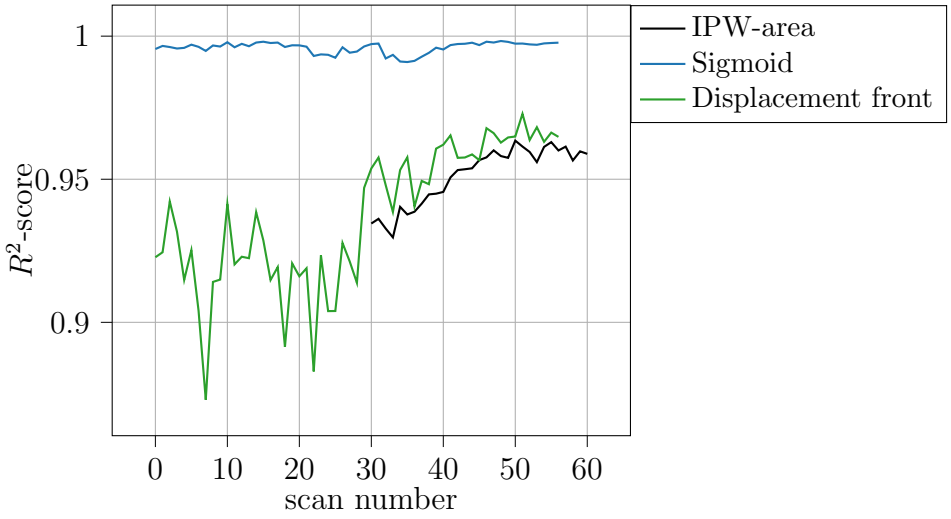

Figure 4.6: The R^2-score for the fitted Sigmoid curves used in the grey value analysis, the 4th-degree polynomial fitted to the displacement front and the hyperbolic paraboloid fitted to the IPW-area.

4.1 Time evolution of the paraffin-air interface

4.1.1 Displacement front - vertical displacement

The grey value analysis serves as a fundamental tool for measuring positions and velocities of the displacement front as it is independent of the segregation quality between paraffin and air. However, it only provides the z-positions of the displacement front. To define the displacement front's location, a reference point is needed on the sigmoid curve. For this, the z-value with the maximum curvature in the upper portion of the sigmoid curves was chosen, illustrated in Fig. 4.7, which would reflect the beginning of the displacement front. The positions as a function of time are showcased in Fig. 4.7a. From these z-positions, the velocities of the displacement front were derived using the central difference for the derivatives[47]. Additionally, a moving weighted average was performed for each time step T_n, using a standard Gaussian distribution as the weighting function. The window size was set to 5, with adjustments made at the boundary points[1]. The results showed a

[1]The weights, w_i, from a standard Gaussian distribution and window size of five is given as $w_{-2} \approx 0.054$, $w_{-1} \approx 0.24$, $w_0 \approx 0.4$, $w_1 \approx 0.24$ and $w_2 \approx 0.054$. Where w_0 is assigned to the centre value.

maximum and minimum velocity of 55 µm/min and 18 µm/min with an average velocity of 36 µm/min. In terms of voxels, these velocities correspond to 9.7, 3.2, and 6.3 voxels per minute, respectively. Fig. 4.7b and Fig. 4.7c present all measured velocities as functions of z and time. Notably, the velocities exhibit relatively rapid fluctuations above $z = 5.9\,\text{mm}$, corresponding to the narrowest area of the pore space, as observed in Fig. 4.1c.

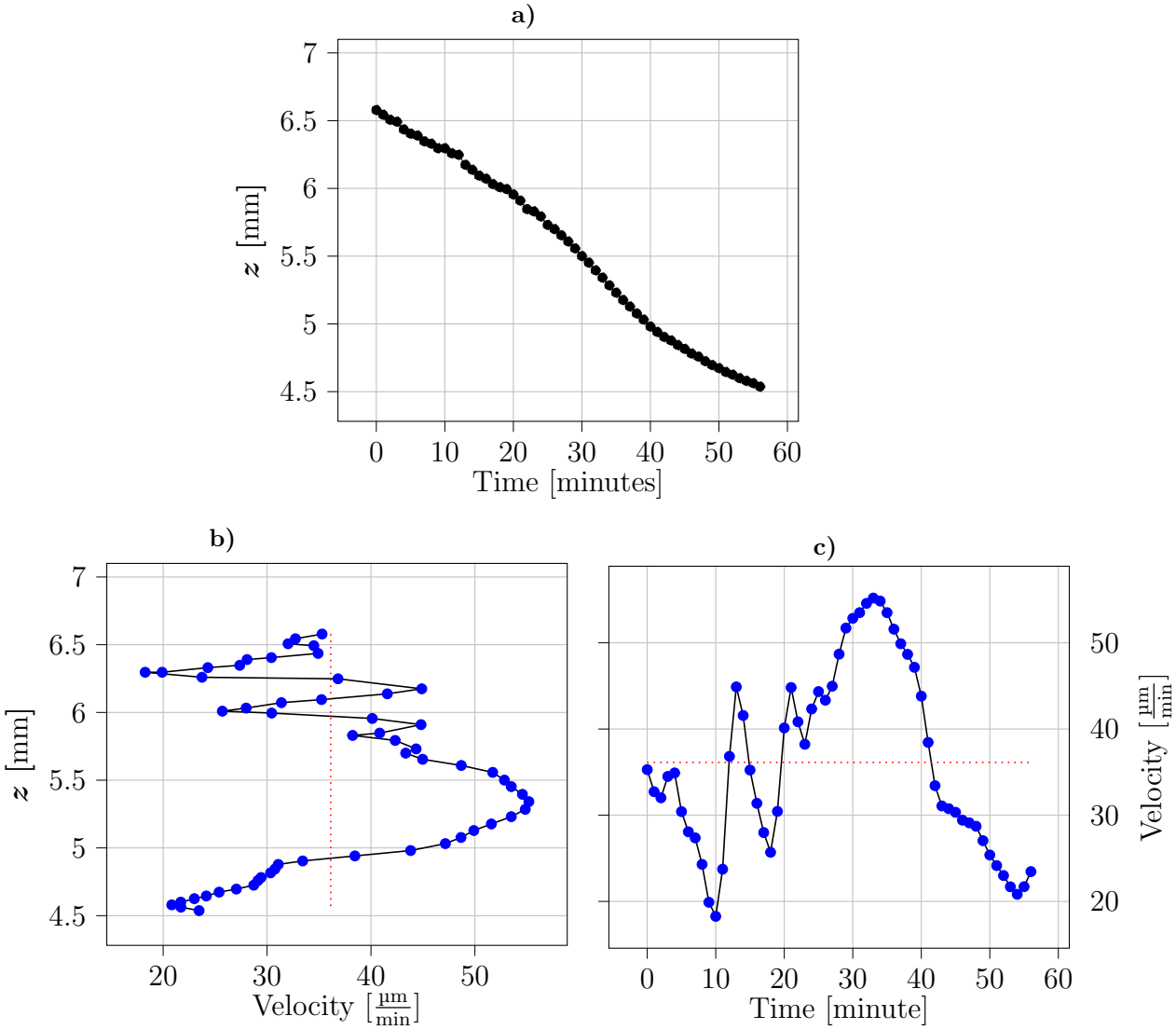

Figure 4.7: The plot in **a)** shows the z-positions of the displacement front for each time step of the experiment, derived from the grey value analysis. The plots in **b)** and **c)** show the derived velocities from the position data. The red dotted line indicates the average velocity at 36 µm/min.

4.1.2 Displacement front - total displacement

To get a complete description of the temporal evolution of the displacement front, the fitted surfaces were utilised. By employing the curvature method for all surfaces, a vector field is obtained, where each vector describes the local velocity of the tracing points on the surface at T_n, as described in section 3.6. The result is depicted in Fig. 4.8, showcasing the complete surface for every 10th time step, along with an

illustration of the width of the surfaces for all time steps. It is evident from, Fig. 4.8 that the width of the surface is influenced by the width of the pore space. Moreover, it reveals that the displacement front tends not to occupy the entire width of the pore space, especially in regions where the pore wall exhibits concave curvature, resulting in the volume closest to the curved pore wall being occupied with paraffin.

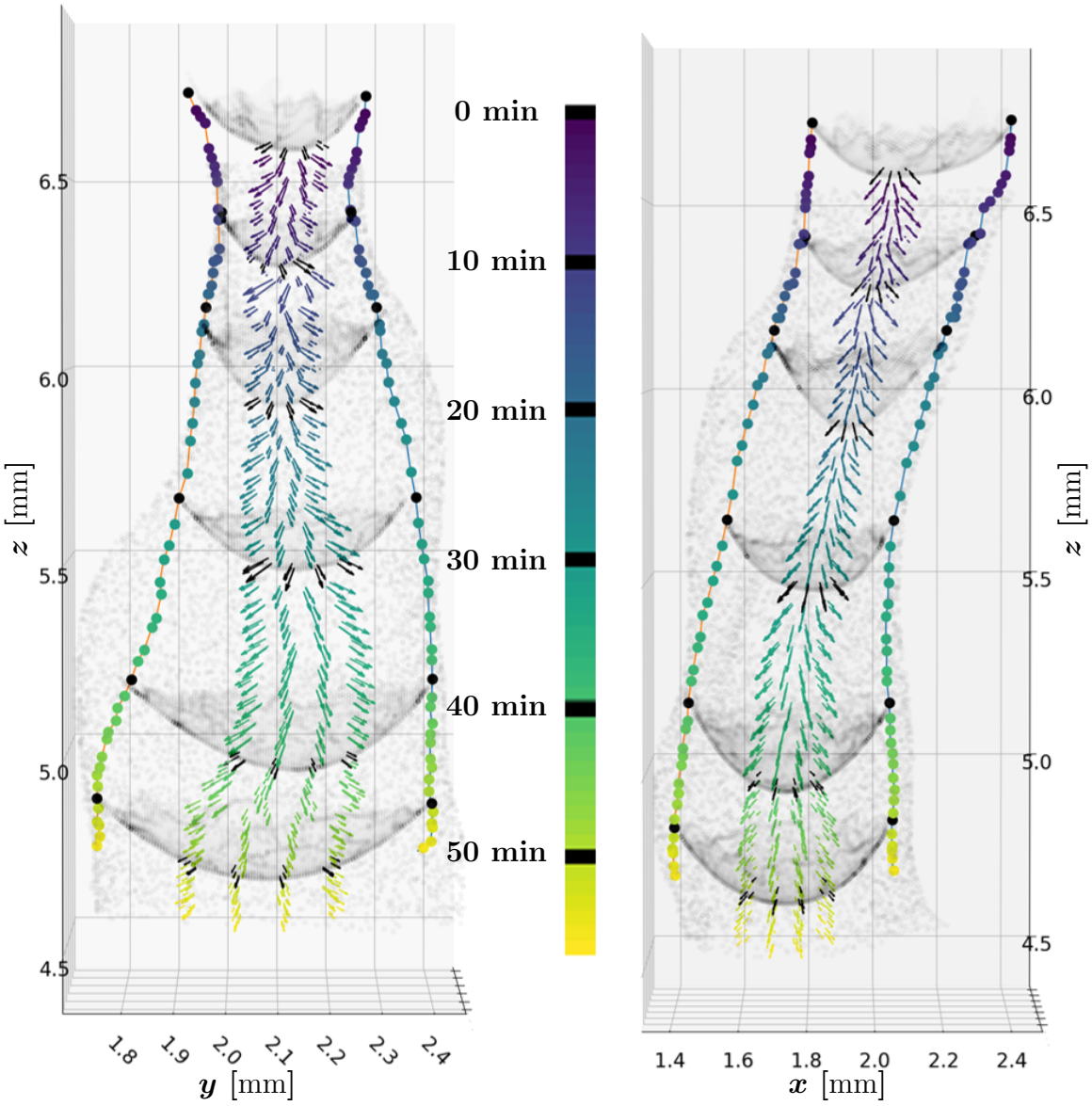

Figure 4.8: Illustrating the time evolution of the displacement fronts through the fitted surfaces. Each time step is assigned a colour from the colour bar, with every 10th time step coloured black for clarity. Additionally, the width of the fitted surfaces is shown using scatter points. The full surface is shown for every 10th time step. Furthermore, each vector corresponds to the velocity of the traced points, calculated using the curvature method. The pore walls are represented with grey scatter points.

It is not clear how to define the total velocity of a surface when the surface undergoes morphological changes between consecutive time steps. This is illustrated by Fig 4.9, which displays the fitted surface for T_{44} and T_{45}. Therefore, both the average velocity and the maximum velocity for all traced points are presented in Fig. 4.10.

Additionally, a moving weighted average, equal to the one used in the grey value analysis (Fig. 4.7b and Fig. 4.7c), was performed for the surface velocities.

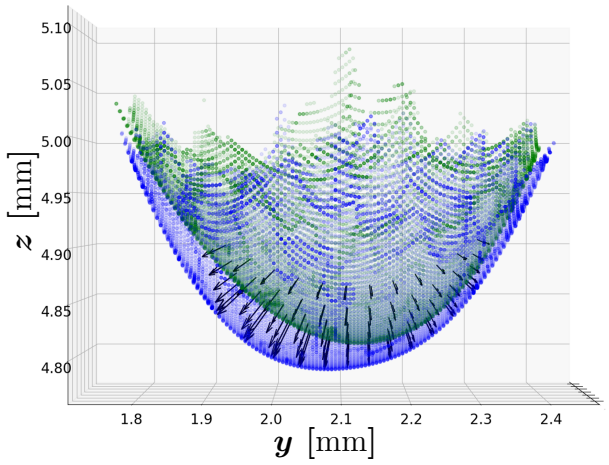

Figure 4.9: Illustrating the shape of two surfaces fitted to two consecutive displacement fronts, green indicating the fitted surface at T_{44} and blue for T_{45}. Each vector is obtained using the curvature method and represents the velocities of the green surface.

The mean maximum velocity of the displacement front was measured at 38 µm/min reaching its peak at T_{30} and minimum at T_{10} with a velocity of 58 µm/min and 27 µm/min, respectively. In terms of voxels, these velocities are measured at 6.7, 10.2 and 4.6 voxels per minute. Compared to the velocities obtained from the grey value analysis, this analysis shows, on average, slightly higher values, since the velocities from the grey value analysis reflect only the z-component of the total velocities. A small difference between the two also indicates that the velocities are mostly dominated by their z-component. It should be noted that the velocities are absolute and do not indicate the displacement direction of the surfaces.

From the average surface velocities, the mean surface velocity was measured at 21 µm/min with the maximum and minimum also at T_{30} and T_{10} with velocities of 33 µm/min and 11 µm/min, respectively. That is 3.7, 5.8 and 1.9 in terms of voxels per minute. The substantial difference compared to the maximum velocities indicates that the velocity of the tracing points varied significantly, indicating that the surfaces did not develop uniformly, as illustrated in Fig 4.9.

To emphasise how the surfaces changed throughout the experiment, the curvatures for the minimum point of each surface were also calculated, demonstrating a fluctuating behaviour before T_{20} and a clear trend of a decreasing curvature throughout the rest of the experiment, as shown in Fig. 4.11. It is worth noting that also the measured velocities exhibit relatively high fluctuations within the first 20 minutes. This occurs between $z = 5.9$ mm and $z = 6.5$ mm, which is located around the smallest cross-sectional pore area at $z = 6.4$ mm shown in Fig. 4.1c.

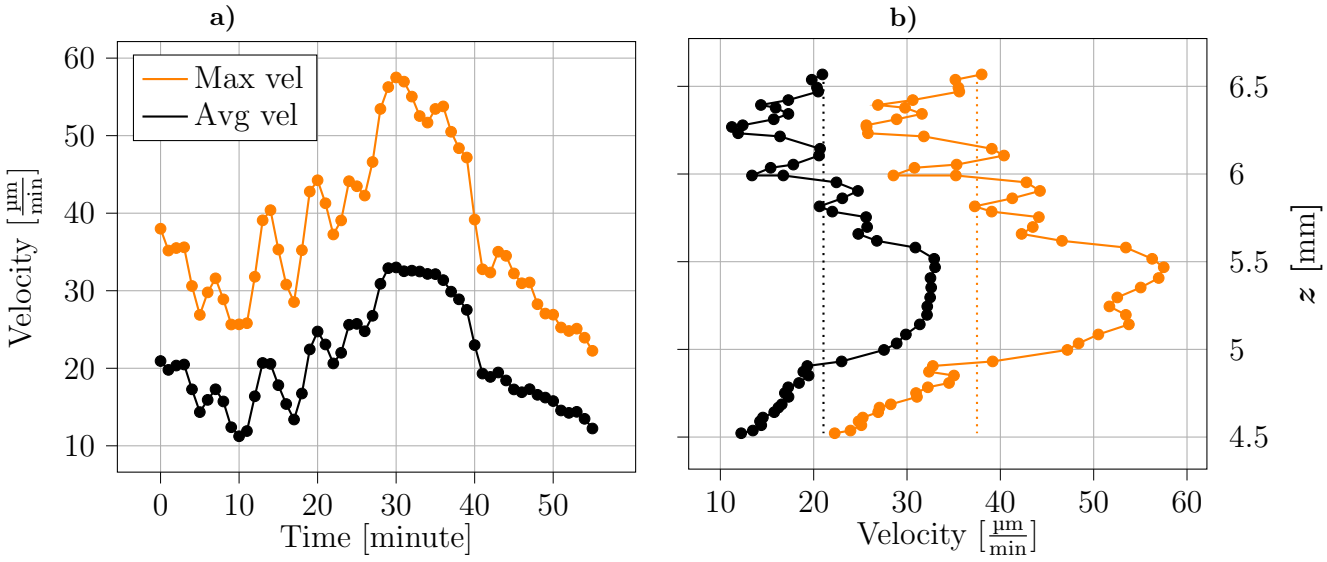

Figure 4.10: The plots in **a)** show the maximum (orange) and average (black) velocity of the displacement front obtained by the curvature method. The plots in **b)** show the same velocities but as a function of z, with the dotted line representing the mean velocities 38 µm/min and 21 µm/min for the maximum and average velocities, respectively.

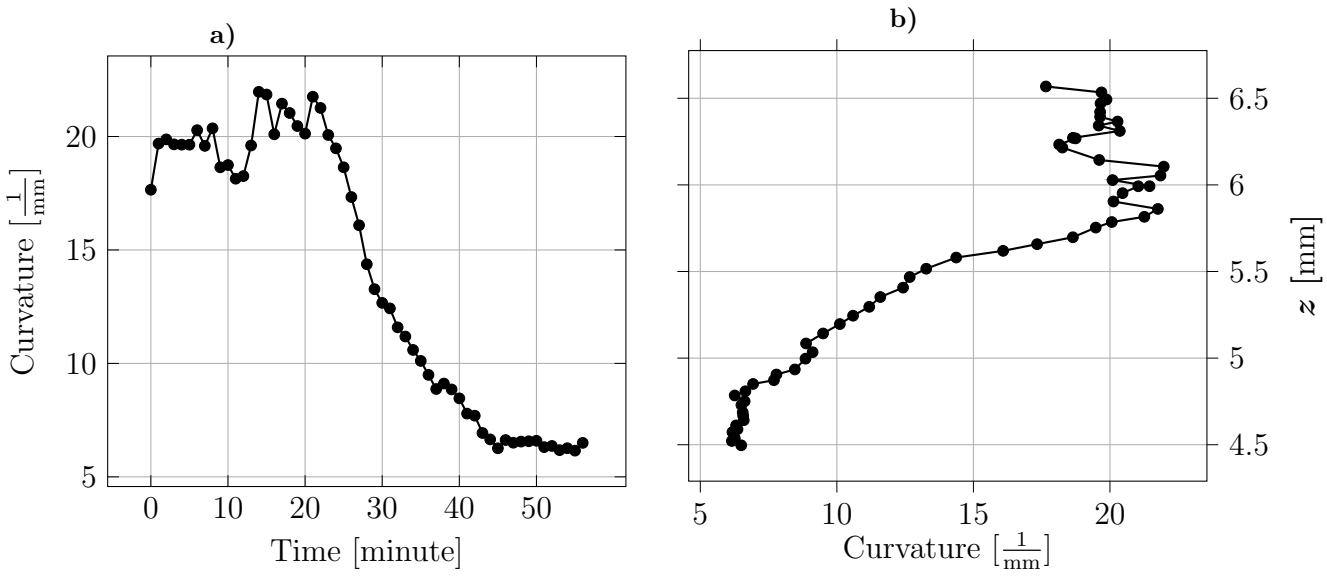

Figure 4.11: Plot **a)** show the curvature measured at the minima of the fitted surfaces for each time step. Plot **b)** shows the same measured curvature as a function of z.

4.1.3 The interface area along the pore wall

To analyse the evolution of the IPW-area, the one-directional method (ref Fig. 3.5) was employed on the fitted hyperbolic paraboloid surface, tracing the movement of the surface along the direction shown in Fig. 4.12b. Notably, Fig. 4.12 demonstrates that the surface exhibits lower velocities towards the edges close to the pore wall compared to the centre of the surface. As a result, the surface curvature increases. Due to the relatively slow evolution of the IPW-area, only every 4th time step is included to illustrate its temporal development, depicted in Fig. 4.13. Each vector in Fig. 4.13 describes the velocity of the fitted surface from T_n to T_{n+4}, starting from T_{27}.

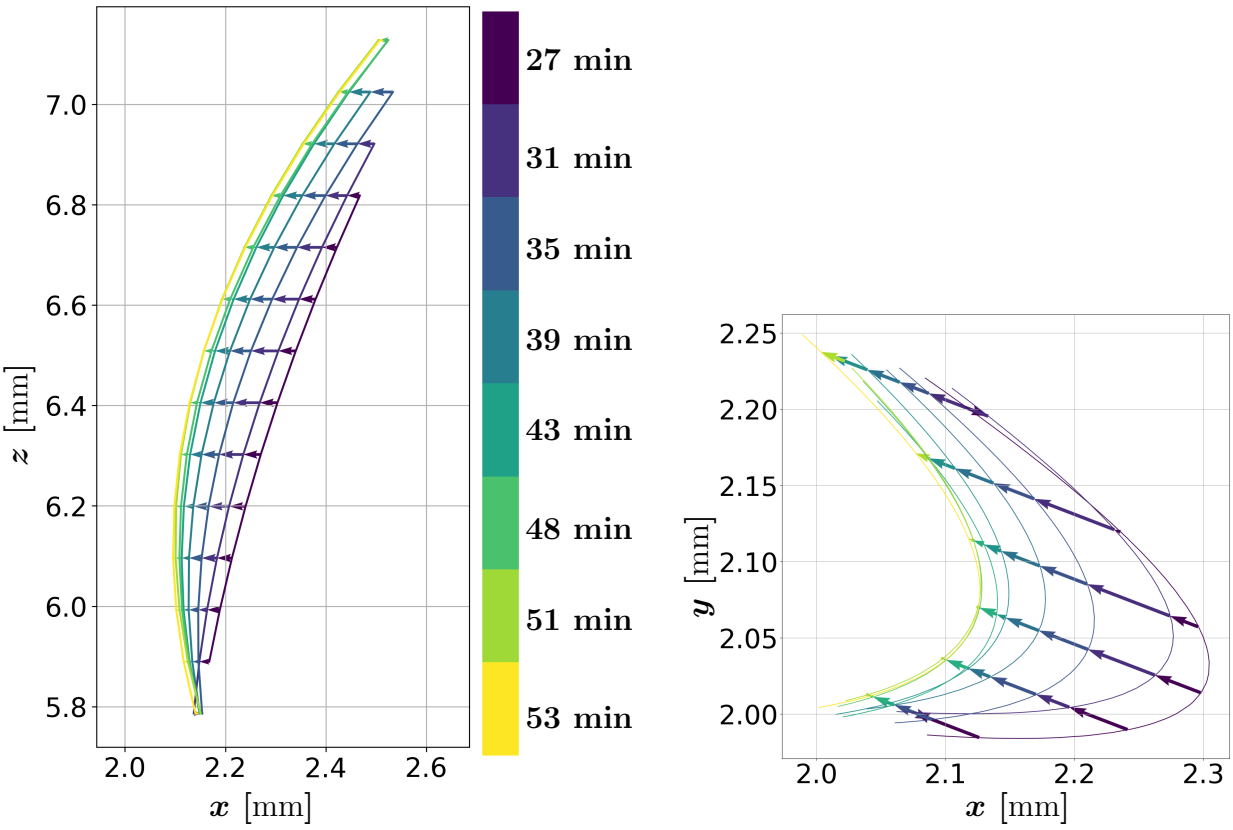

a) *xz-plane at* $y = 2\,\text{mm}$. **b)** *xy-plane at* $z = 6.4\,\text{mm}$.

Figure 4.12: Illustrating a slice of the IPW-area and the velocity vectors calculated by the one-directional method. Each time step is assigned a colour from the colour bar.

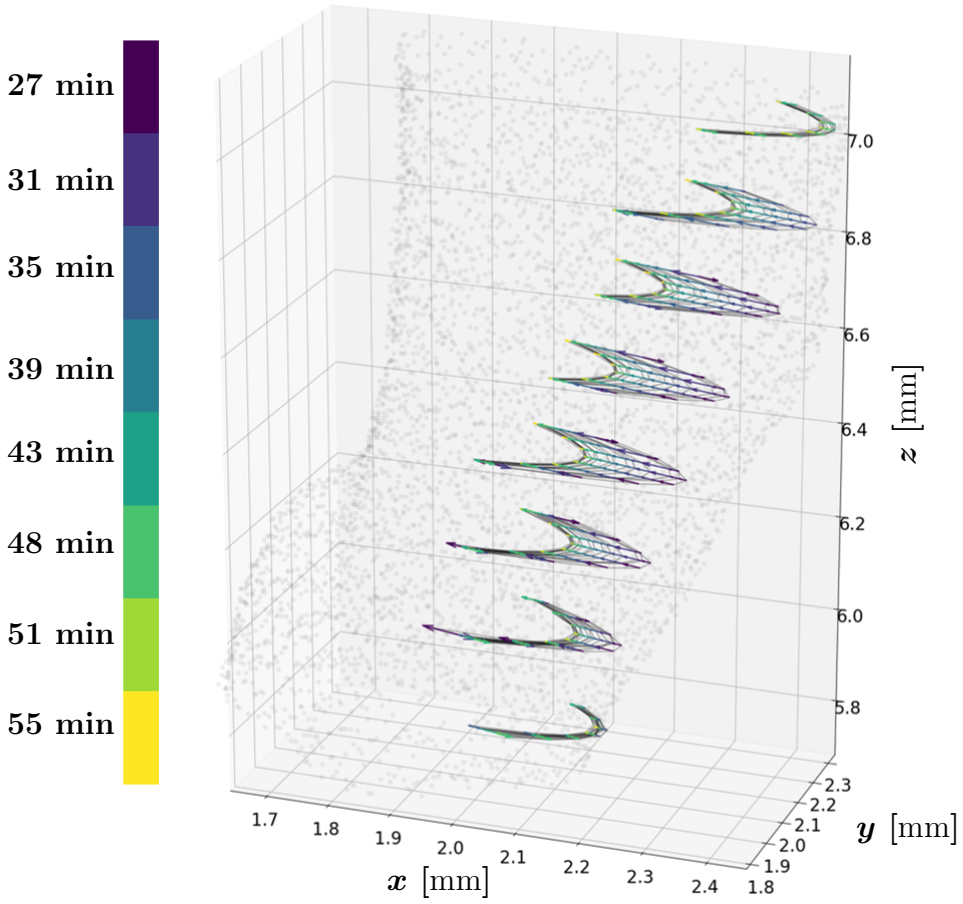

Figure 4.13: Depicting the time evolution of the IPW-area through the fitted surfaces using every 4th time step. Each time step is assigned a colour from the colour bar. Grey lines are also drawn between the velocity vectors belonging to the same time step to get a better illustration of the shape. The pore wall is depicted with grey scatter points.

Two different grids of tracing points were used to calculate the velocities using the one-directional method. To mitigate the impact of random fluctuations, velocities were calculated using only every other time step, and a moving weighted average, as used in the grey value analysis (ref section 4.1.1), was utilised.

The first grid covered the entire surface area of the IPW-area. By taking the average velocity for each time step, the results shown in Fig. 4.14 were obtained. From it, it is clear that the velocities accelerated towards the maximum velocity measured 7 µm/min, hence 1.2 voxels per minute, in the 33-35 time period, with the velocities decreasing towards 0 throughout the rest of the experiment.

Observing Fig. 4.12a and Fig. 4.13, it is noticeable that the surface curves, with the highest velocities measured towards the centre of the IPW-area. For that reason, a new grid of tracing points was utilised, explicitly covering the central region of the IPW-area between $z = 6.35$ mm and $z = 6.65$ mm. The average velocities from this grid showed the same behaviour as when tracing the entire surface area, but with the velocity peaking at T_{33} with 13 µm/min, hence 2.3 voxels per minute.

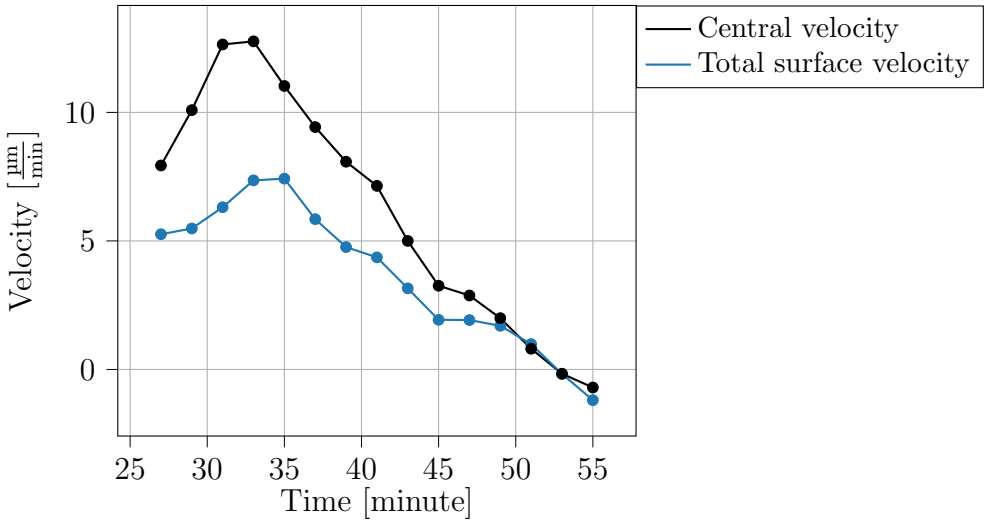

Figure 4.14: The velocities of the IPW-area using the one-directional method on a grid covering the entire surface and a grid only covering the central region of the surfaces.

4.2 Analysing the quality of the fitted surfaces to the displacement front

The analysis of the residuals, as described in section 3.7, revealed that 0.64% of the fluid interface voxels belonging to the displacement front were classified as outliers, with a residual distance greater than 3σ. This value is more than twice the expected rate of 0.3%, assuming the interface points to be random from a normal distribution on the fitted surface. This suggests that the assumed parabolic shape fails to capture some of the morphology of the fluid interface.

To further investigate this, the orientation of the outliers relative to the surface minima in the xy-plane was mapped. The results, depicted in Fig. 4.15, indicate that the outliers are predominantly observed in the $(-x, -y)$ quadrant of the plane (see Fig. 4.8 for reference).

The same analysis was performed, but then classifying all fluid interface voxels with residuals greater than 2 times the standard deviation of the residual distribution. A similar pattern is observed here, showing that the classified interface voxels occur more frequently in the $(-x, -y)$ quadrant of the plane.

To further investigate if the fitted surfaces fail to capture any features or anomalies of the displacement fronts, a search for consecutive clusters of outliers appearing in the relatively same positions was performed. A notable result was observed between T_0 and T_3, where a cluster of outliers appeared in the same position for four consecutive time steps. This cluster is marked in blue in Fig. 4.16. However, the size of the clusters were not significant enough for further investigation.

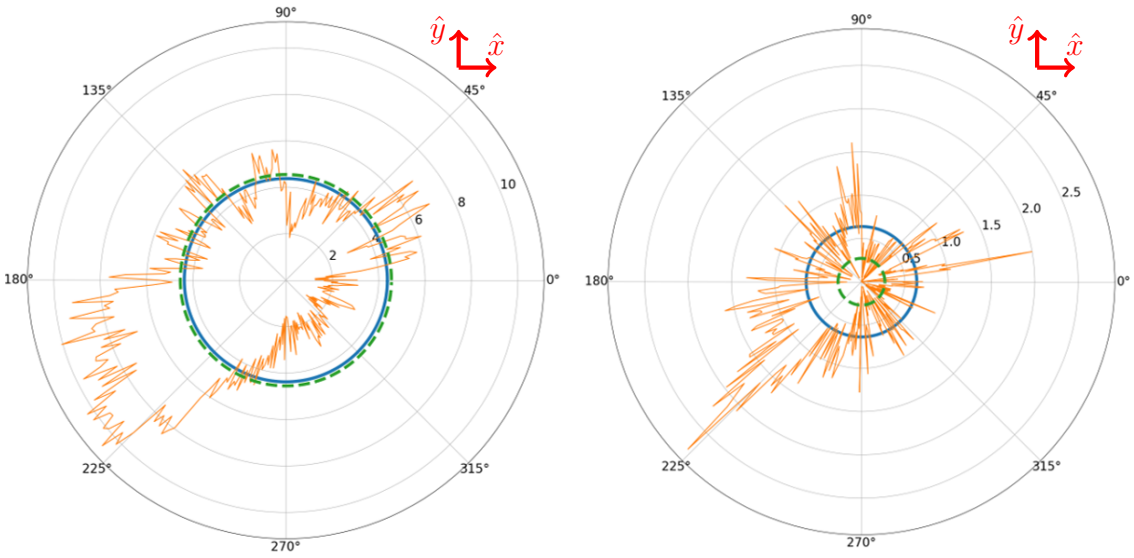

a) *Outliers with residuals greater than* 2σ. **b)** *Outliers with residuals greater than* 3σ.

Figure 4.15: **a)** and **b)** shows the ratio of outliers for each angle relative to the minima of the displacement fronts. The blue circle indicates the total measured ratio of outliers, and the green circle indicates the expected ratio of outliers, which is 4.55% for **a)**, and 0.3% for **b)**.

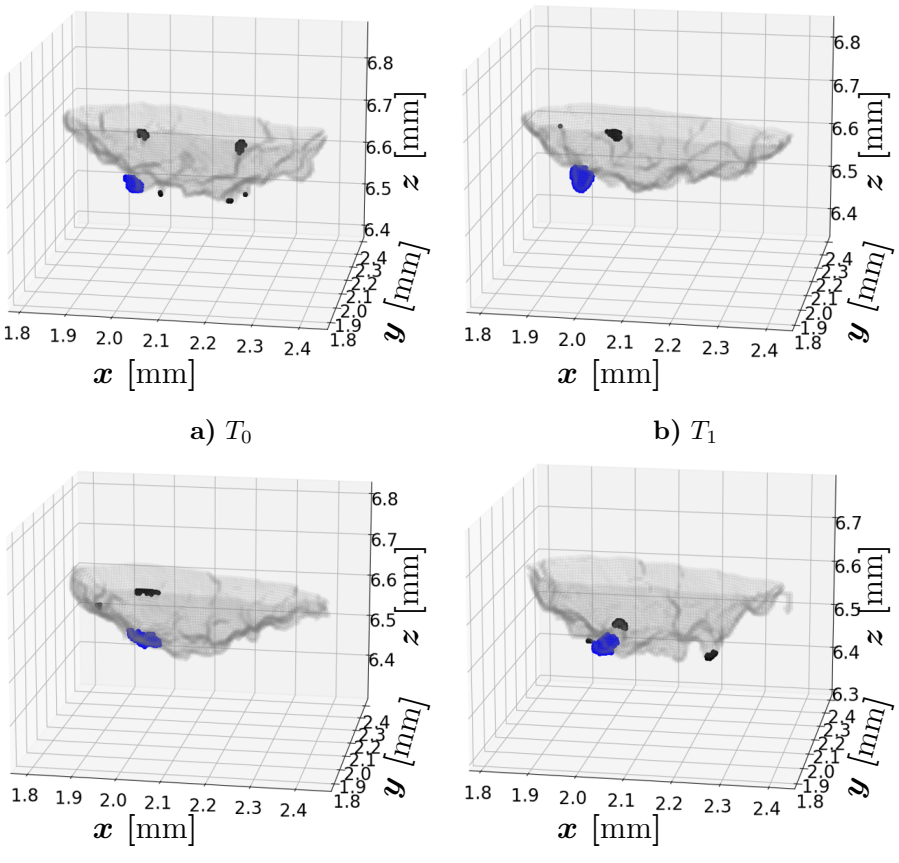

a) T_0 **b)** T_1

c) T_2 **d)** T_3

Figure 4.16: The displacement front for T_0 to T_3, highlighting all outliers with black colour and the cluster of interest with blue colour. For the cluster of interest is also the neighbouring outliers with residuals greater than 2σ marked with blue.

4.3 Overview of the entire pore space throughout the experiment

To get a better overview of how the fluid interface developed throughout the experiment, the volume of air in the system for each time step was measured, shown in Fig. 4.17. The measurements showed a relatively linear increase in the volume of air in the system with an average of 6.5 nL entering the system per minute. Although a constant pump rate is expected, this is probably evidence that the pump rate changed around T_{30} and T_{35}, with an average pump rate of 4.4 nL/min before T_{30} and 6.9 nL/min after T_{35}.

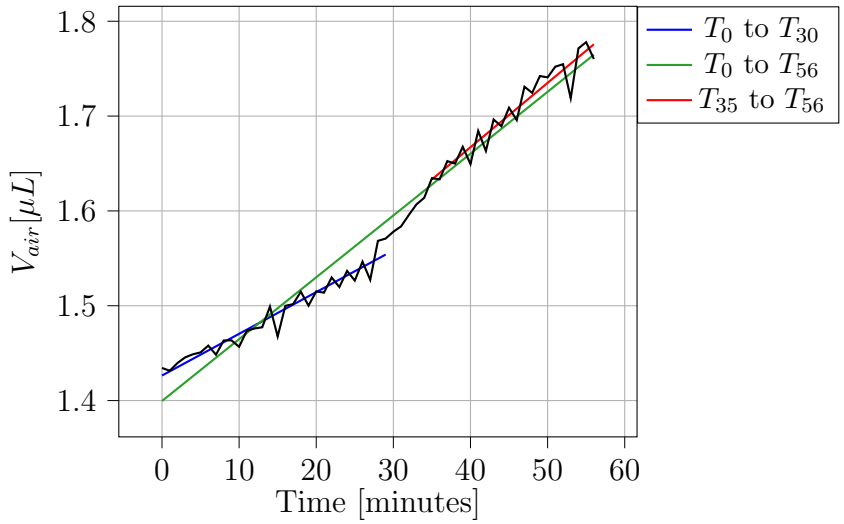

Figure 4.17: The volume of air in the pore system as a function of time, along with fitted lines for the volume measurements between, T_0 and T_{56} in green, T_0 and T_{30} in blue, and T_{35} and T_{56} in red, with the corresponding slopes of 6.5 nL/min, 4.4 nL/min and 6.9 nL/min, respectively.

The surface area of the fluid interface is affected by the paraffin moving upstream along the pore walls. In Fig. 4.18, two different slices of the system are shown, illustrating how the fluid interface changes over the course of the experiment. It is evident from the images that the interface is characterised by noise, making a simple calculation of the surface area prone to overestimation. To mitigate this effect, the ratio of the fluid interface surface area to the surface area of the pore wall was calculated instead. An increase in this ratio throughout the experiment would then suggest an increase in fluid interface area, which Fig. 4.18c does indicate. This observation is further supported by Fig. 4.19, which displays the pore system at the initial time step (T_0) and the final time step (T_{56}) of the experiment. From Fig. 4.19, it is also noteworthy that a cavity far up in the pore system has been partially filled with paraffin throughout the experiment. Comparing to Fig. 4.2b, this did not start before after T_{30}.

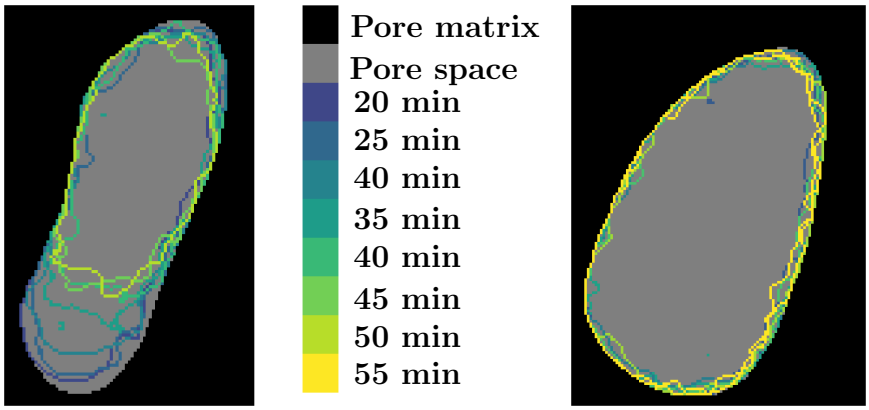

a) *Cross-section of the pore at* $z = 6.8\,\text{mm}$

b) *Cross-section of the pore at* $z = 7.3\,\text{mm}$

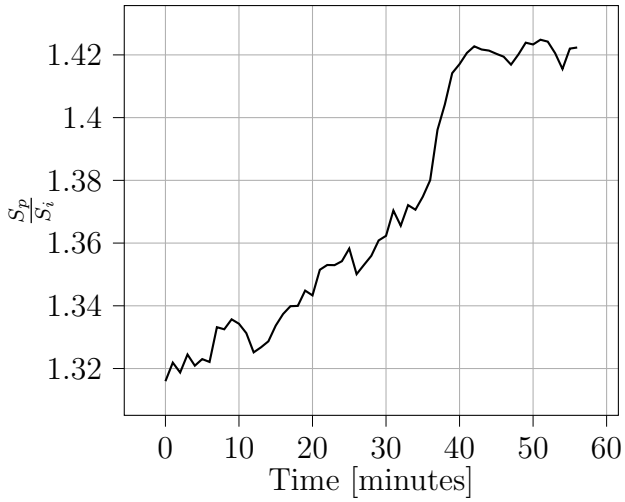

c) *Ratio between the surface area of the pore wall,* S_p*, and the fluid interface area,* S_i

Figure 4.18: **a)** and **b)** illustrating the fluid interface for the time steps corresponding to the colour bar for two different cross-sections of the pore space. **c)** gives an indirect measurement of how the fluid interface surface area between air and paraffin changes throughout the experiment.

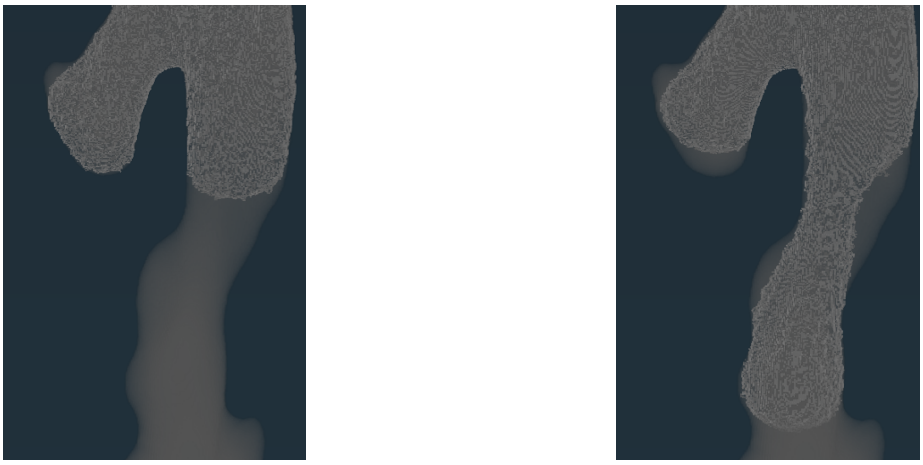

a) T_0

b) T_{56}

Figure 4.19: Illustrating the pore space with air (light grey) and paraffin (dark grey) at the beginning and the end of the experiment.

Chapter 5

Discussion

The primary objective of this experiment was to explore the capabilities of the CT scanner and determine if a time-resolved dataset could be obtained. The criterion for a time-resolved dataset is that all captured displacements are below three voxels per time step, meaning that the resolution is no longer dependent on the temporal resolution but rather the spatial resolution. With a voxel size of 5.68 µm and a time step length of 1 minute, this criterion would correspond to velocities below 17 µm/min. Based on the measured velocities of the displacement front, it is evident that the criterion for a time-resolved dataset is not fully met as most of the velocities in Fig. 4.10 exceeds this criterion. Nonetheless, in the IPW-area, all velocities were measured below 17 µm/min, with even the maximum velocity measured at 12 µm/min. Therefore, it is concluded that the experiment only achieved a partially time-resolved dataset.

The velocities of the fluid interface were influenced not only by the pressure difference caused by the paraffin drainage but also notably by multidirectional forces where the paraffin flow is most predominant close to the air. In general, this gave rise to two distinct characteristic movements of the fluid interface: The downward motion of the displacement front and the horizontal motion observed for areas such as the IPW-area, leading to a narrowing of the air pathway, as Fig. 4.2c illustrate, which consequently increased the overall fluid interface surface area as indicated by Fig. 4.18c.

Mathematical surfaces were fitted to the regions of interest to describe the temporal evolution of the fluid interface. The choice of using a parabolic surface for the displacement front and a hyperbolic surface for the IPW-area was guided by the assumption that the wetting properties between the paraffin and the Epoxy Resin-based pore matrix would influence the morphology of the fluid interface. As the air was drawn into the system, the paraffin would accumulate near the pore walls, causing the air to be concentrated in the central region of the pore space. Additionally, the relative laminar flow of the paraffin was anticipated to result in a smooth interface.

These assumptions proved to describe the IPW-area exceptionally well, reflected by the high average R^2-score of 0.95, meaning that the assumed hyperbolic surface

explains 95% of the variability. The remaining 5% is attributed to the boundaries of the IPW-area, which Fig 4.5b shows does not have an optimal fit. A search for anomalies was also performed by analysing the residual distance from the fluid interface points to the fitted surface. However, contrary to the displacement front, no anomalies were detected. As the velocities were relatively slow, shown in Fig. 4.14, one can conclude that the surface development had a high temporal resolution, indicating that any anomalies from the hyperbolic surface assumption are, at worst, limited by the spatial resolution.

In contrast to the IPW-area, the analysis of the displacement front and its fitted parabolic surfaces revealed that the assumed parabolic shape alone was an insufficient description. The presence of anomalies in the fluid interface became evident from the ratio of outliers and their consistent appearance in the $(-x, -y)$ quadrant of the pore space, as shown in Fig. 4.15. The R^2-score, shown in Fig. 4.6, indicated that, on average, the parabolic shape could explain approximately 93% of the variability. However, when examining the R^2-score prior to T_{30}, this number decreased to 91%. While these are relatively high scores, there remains a portion of the variability that cannot be attributed to the parabolic shape and is likely associated with these anomalies.

Although anomalies in the displacement front were detected, the experiment's limited spatiotemporal resolution prevented a more in-depth understanding. The relatively high velocity of the displacement front suggests that the primary cause of this limitation is the temporal resolution. However, the frequent appearances of the anomalies in the $(-x, -y)$ quadrant are understood by observing the pathway of the displacement front in Fig. 4.8, where it is evident that this area is predominantly influenced by an upstream flow of paraffin along the pore wall. This provides a natural explanation for the high rate of anomalies occurring in this region, as the velocity of the air relative to the paraffin is higher, resulting in a less stable or deformed displacement front. It is worth noting that each CT scan captures the average state of the system over a 40-second time period. Therefore, the systematic anomalies in the displacement front indicate either slow-changing variations or systematic rapid fluctuations. Fig. 4.16 further suggests that these anomalies can persist for several minutes.

An important concept to understand when deriving the velocity of an object rendered by voxels is that its displacement is measured as the average displacement of all voxels defining that object. If a single voxel represents the object, one could only derive integer-valued displacements, one voxel per time step, two voxels per time step etc. At this level, the uncertainty would also be high. At its worst, a small object relative to the voxel size may exhibit a displacement close to an entire voxel without it being measured. This effect is negligible for our measured velocities as both the displacement front and the IPW-area are rendered by a significant amount of voxel. If the spatial resolution is low, however, this effect becomes more significant, especially for smaller objects, such as the clusters of outliers showcased in Fig. 4.16. This is part of the reason why it was not possible to extract more information about the anomalies. This also provides additional motivation for fitting smooth surfaces to the fluid interface points. By using a surface that represents an average of the fluid interface point, local velocities can be extrapolated from the

surface.

The main developments in this system occur at the displacement front. Its velocities are derived by the curvature method and shown in Fig. 4.10, and the validity of these results is strengthened by the more simple grey value analysis method, which only analyses the grey values of the filtered tomograms, reflecting only the z-component of the total velocity. Nevertheless, as the velocities of the displacement front are most predominant by its z-component, the same velocity development is apparent in both Fig. 4.7 and Fig. 4.10. Three temporal intervals emerge as notable. In the first period, between T_0 and T_{20}, the velocities seem to fluctuate. This occurs when the displacement front is located between $z = 6.6\,\text{mm}$ and $z = 5.9\,\text{mm}$, which is the smallest section of the pore space. Intuitively one would then expect that the highest velocities would be measured here. However, one needs to recall that the pump rate is extremely low and that the paraffin close to the wall is seemingly experiencing an upwards force throughout the experiment. The displacement front will, therefore, in a confined pore area, be affected by two competing forces. This may result in unstable and fluctuating behaviour of the displacement front, and that the pressure in the system builds up. This fluctuation is consistent with both the measurements of the curvatures and the velocities shown in Fig. 4.10 and Fig. 4.11.

After T_{20}, the velocities stabilise, and the displacement front accelerates towards its highest measured velocities between T_{28} and T_{39}. This occurs between $z = 5.5\,\text{mm}$ and $z = 5.0\,\text{mm}$ where the cross-sectional pore area is above average, as seen in Fig. 4.1c. Two factors should be considered here. Firstly, the effective size of the displacement front is not fully correlated with the pore size, as the presence of paraffin affects the available space, illustrated in Fig. 4.8. Secondly, it is noteworthy that the IPW-area also exhibits its velocity peak during this time frame, indicating a rapid increase in the volume of paraffin in that region. Overall, the rate of change of the paraffin-air interface surface area is also at its maximum in this time frame, demonstrated in Fig. 4.18c. These observations suggest that the rate of paraffin passing the displacement front increases and is most likely due to a pressure drop in the smallest pore area, which was built up before T_{20}. This pressure drop results in a forced downward movement of air as paraffin escapes upward, explaining the peak velocities observed during this time period.

During the last time period from T_{40} to T_{56}, a decrease in the measured velocities of the displacement front is observed. This decrease coincides with the expansion of the displacement front, as it covers more of the width of the pore space. The growth of the fluid interface surface area also stagnates, as seen in Fig. 4.18c, along with the velocities measured for the IPW-area, seen in Fig. 4.14. This indicates that the retrograded motion of the paraffin has stagnated. Evidently, the cross-sectional pore area becomes the determining factor for the velocity of the displacement front positioned between $z = 5.0\,\text{mm}$ and $z = 4.5\,\text{mm}$ in this time period, which Fig. 4.1c shows is the largest cross-sectional pore area.

5.1 Assessing the method used to derive the velocities

As mentioned in section 4.1.2, defining the velocities between two consecutive surfaces representing the displacement front is not trivial, as exemplified in Fig. 4.9. The approach adopted for the curvature method assumed a radial growth for the tracing points on the surfaces, based on the idea that a displacement front at T_n grows into its new position at T_{n+1}. Hence, it is expected that the displacement of the surface from T_n to T_{n+1} is most predominant close to the minima where the curvature method is most accurate and less towards the edges. This behaviour was verified by visually inspecting each time step, justifying the use of the curvature method, and placing the tracing points in close proximity to the minima of the fitted surface. Fig. 5.1 gives two additional examples of two consecutive time steps to show this. Alternative methods were also tested. Such as assuming that all tracing points on the surface did not evolve radially but rather parallel to each other. The direction of the tracing points could then be found by tracing the minima of the displacement front at T_n onto the following minima at T_{n+1}. However, this method was found to be less robust than expected as it was too sensitive to morphological changes of the displacement front and, therefore, not used in the analysis.

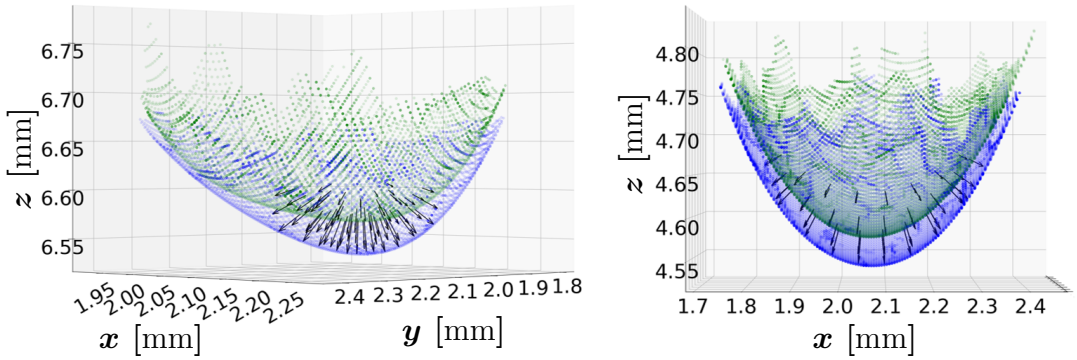

a) T_0 *and* T_1. **b)** T_{53} *and* T_{54}.

Figure 5.1: Two examples of two consecutive fitted surfaces. Green indicates the fitted surface at T_n and blue for T_{n+1}. Each vector is obtained using the curvature method and represents the velocities of the green surface.

The one-directional method worked well when tracing the development of the IPW-area, as it was able to capture both the morphological development of the surface as well as its growth throughout the experiment. It was, however, sensitive towards the boundaries, as the assumed hyperbolic shape did not accurately describe the boundaries at the paraffin-air-matrix interface. The velocities closest to this interface were therefore ignored. It should be mentioned that a general weak spot for the one-directional method is when the surfaces do not actually develop in one direction. However, Fig. 4.12b does illustrate that this is not the case for the IPW-area, validating the use of the method.

Regarding the grey value analysis, a reference point on the sigmoid curves was required to determine the velocities. This reference point was chosen to be as close as possible to the corresponding minima of the fitted surface so that the positions

in Fig. 4.7 and Fig. 4.10 could be compared. Additionally, this choice of position was less affected if the displacement front stretched longer along the z-direction, which can occur if the ratio of paraffin and air for each cross-section changes more gradually, as observed in the case of T_{30} as shown in Fig. 4.2b.

5.2 Setup

A suitable test sample was necessary to replicate the characteristics of a real pore system while maintaining simplicity so that the fluid velocities could be controlled effectively during the experiment. Through previous work, such a test sample had already been developed, which inspired the test sample used in this experiment with the additional modifications of adding the funnel and aligning the pore space with the rotational axis of the embedding cylinder[1]. Indeed, tailoring the test sample was essential to mitigate certain weaknesses of fast CT imaging. The lack of sharp edges made it possible to use fewer projections as these, in general, demand more projections to be accurately reconstructed. Furthermore, aligning the pore space close to the rotational axis of the cylinder reduced blurring effects that occur from higher tangential velocity further from the centre of rotation. Additionally, by adopting a simplified morphology for the pore system, both the analysis process and the fluid control became more manageable.

A constant difficulty of the experiment was to avoid unstable air bobbles being captured inside the pore system, as these could cause sudden, unpredictable changes to the fluid interface mid-experiment. One of the measures taken to cope with this was to initially flush the system with paraffin at a high pump rate and slowly drain the system for paraffin during the image acquisition. A consequence of this is that the pore walls would be coated with paraffin from the beginning of the experiment. This could give some explanation for why the retrograded motion of the paraffin was so dominant throughout the experiment. It could also explain why the cavity in Fig. 4.19b could be refiled with paraffin late in the experiment as it was connected with the paraffin further down in the system through the thin paraffin film along the pore wall.

The crux of the experimental setup was to facilitate a steady flow of fluids that could be controlled throughout the image acquisition process. To achieve this, a pump was designed specifically for the experiment, capable of pumping small volumes of paraffin while meeting the practical requirements necessary for it to function during multiple consecutive rotations of the CT system's rotating stage. A rough estimate of the required pump rate shows that the pump needed to be capable of pumping 2.2 nL/min to maintain fluid velocities below three voxels per minute. The estimate is based on a simplified system, illustrated in Fig. 5.2, where the system is viewed as a cylinder with a cross-sectional area equal to 0.13 mm^2, hence the minimum cross-sectional area measured for the pore space. To maintain the fluid interface velocity at 17 µm/min, hence three voxels per minute, the pump rate needed to be 2.2 nL/min.

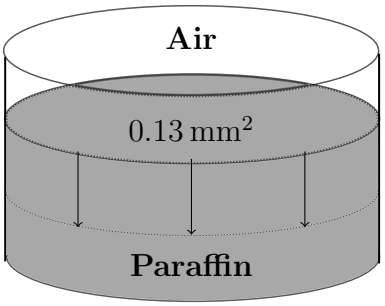

Figure 5.2: Illustrating a cylinder with a cross-sectional area of $0.13\,\mathrm{mm}^2$ where the fluid interface is moving downwards.

The estimated pumping capacity of the pump was approximately 2.5 nL/min, which theoretically should have been sufficient to maintain acceptable fluid velocities in the majority of the pore space. However, during tests, it was observed that the pump suffered from some leakage, possibly due to imperfections in the syringe or the transportation system from the syringe to the sample holder. Tests also showed that the exact amount of leakage was unpredictable but relatively stable if the pump rate was not altered. To address the issue, the pump was set to inject paraffin at a rate of 10 nL/min, offsetting some of the leakages. As a result, the net pump rate was found to be 6.5 nL/min when paraffin was being drained from the system. It is clear that this net pump rate was insufficient based on our initial estimates, which also showed during the analysis of the experiment. Some evidence also suggested a minor change in the amount of air entering the system at T_{30}, as shown in Fig. 4.17. This change could indeed be attributed to a variation in the pump rate, which could be caused by a change in the rate of leakage or, as previously argued, that the pressure difference caused by the pump was counteracted by paraffin-resin wetting properties, giving a lower measure on the pump rate.

5.3 Imaging and filtering

In this experiment, 80 projections were chosen for each scan, with an exposure time of 0.5 seconds per projection, resulting in a total acquisition time of 40 seconds. The choice of these parameters was based on the previous work leading up to this experiment, where it was found that 85 projections provided the best trade-off between a low acquisition time and spatial resolution[1]. However, by aligning the pore space to the centre of rotation of the cylinder, fewer reconstruction errors were expected, and since the temporal resolution was prioritised in the experiment, the number of projections was reduced to 80.

The acquisition time of precisely 40 seconds was not coincidental but rather constrained by the velocity limit of the rotating stage. If there were no such limitations, alternative strategies could have been employed to achieve better spatiotemporal resolution. One possible approach would be to hard bin the detector pixels, where adjacent detector pixels are merged, giving a larger pixel size but a better signal-to-noise ratio. Given the inherently low signal-to-noise ratio in fast imaging, it could be argued that a voxel size of 5.7 µm is superfluous. By increasing the signal-to-noise ratio through hard binning, the exposure time could be reduced, with the net result

of an improved spatiotemporal resolution.

A time constraint that did not affect the imaging itself but only contributed to a worse temporal resolution was the enforced 20-second resting time between each scan. This was a supplier software limitation and did not contribute to anything other than an increase in the time step length. Although too late for this experiment, this issue was resolved. With this in place, one can estimate a 33% improvement in the temporal resolution if the experiment was to be repeated, with no cost of the spatial resolution.

An essential aspect of the analysis in this experiment is the accurate alignment of the 57 individual scans to ensure a reliable comparison. Misalignment could occur if the test sample's position changed, which there was no indication of, or if there were variations in starting angle of the rotating stage, which was observed. Due to unreliable angle measurements from the Nikon system, the preferred approach was to align the images using a small metal piece as the reference point, shown in Fig. 5.3. Exploiting the substantial contrast difference to the Epoxy Resin and calculating the average position of the voxels belonging to the metal piece, the relative starting angle for each tomogram could be approximated, shown in Fig. 5.4. The uncertainty in this method is in the localisation of the metal piece, which may result in a less-than-perfect alignment. However, this is considered negligible for the analysis of the fluid interface, as the analysis area, shown in Fig. 4.1, was located relatively close to the centre of rotation, minimising the effects of small angular variations. The surface and volume analysis, on the other hand, could be more affected as they rely on proper alignment with the mask for the entire pore space. Misalignment in these analyses could lead to underestimation of the air volume, as illustrated in Fig. 5.5, which could explain some of the more significant dips observed in the volume of air entering the system, shown in Fig. 4.17, such as the one seen at T_{53}.

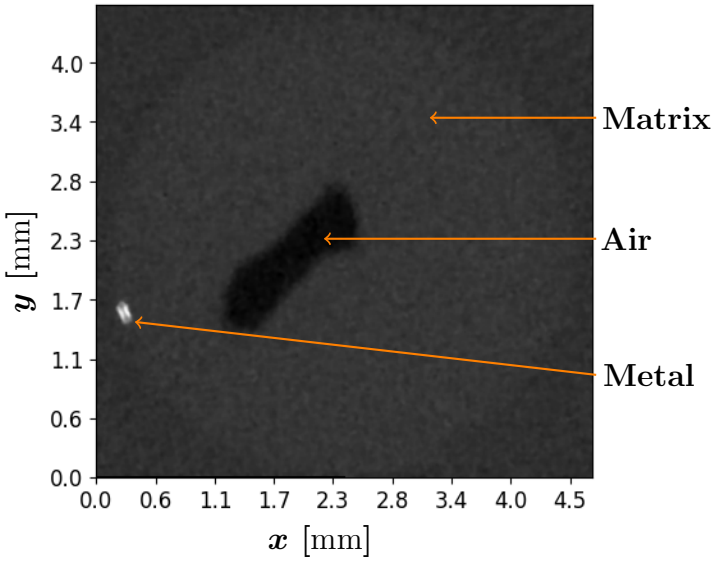

Figure 5.3: Illustrating cross-section of the pore system and the contrast between air, matrix, and the metal piece.

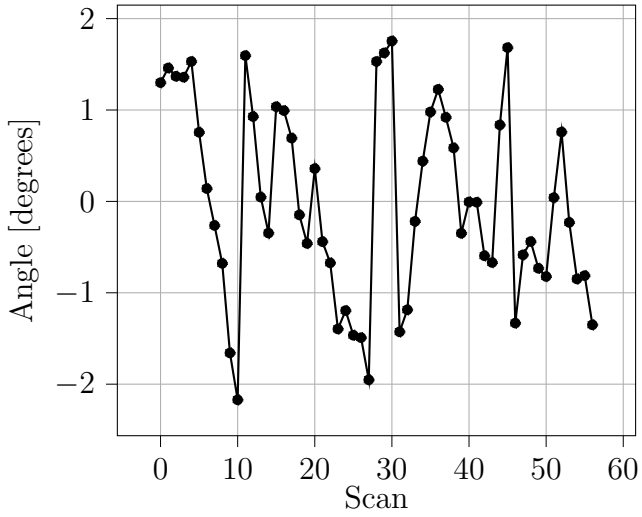

Figure 5.4: Showcasing the relative angular orientation for each tomogram before aligning them.

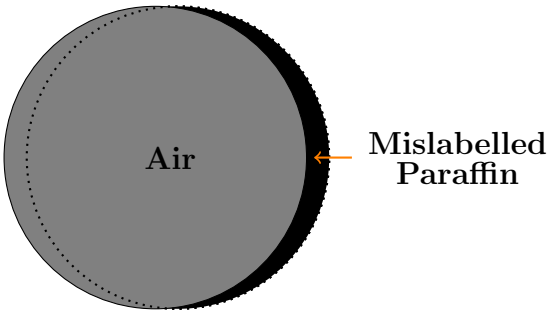

Figure 5.5: Illustrating the mask, marked as a dotted circle, and the pore space filled with air, marked with a grey circle. A misalignment between the two will cause the measured volume of air to be reduced, giving the impression that some of the space is filled with paraffin.

All CT scans were performed with the same parameters, and applying the same filtering to them is, therefore, natural. Both the median filter and the Non-local mean filter were selected to act relatively aggressively on the images, as the signal-to-noise ratio was relatively high. A consequence of this is that boundaries in the images become more blurred, which can affect the morphology of the fluid interface. However, using the ground truth, a high-resolution tomogram of the sample without any liquids as a mask, the effect can somewhat be neglected for the interface between fluid and pore matrix, but it can not be neglected for the fluid-fluid interface. To understand the influence of both filtering and a generally low signal-to-noise ratio, two independent approaches were used.

The first approach was to use the residual distances from the displacement front to its corresponding fitted surface, resulting in the distribution shown in Fig. 5.6, with a standard deviation of 2.4 voxels. It has, however, been indicated that the parabolic shape was not fully descriptive of the displacement front. Features not captured by the approximated parabolic shape will therefore increase this standard deviation.

The second approach assumed that the threshold method used to separate the two fluids would have a similar effect when separating matrix and air. A valid assumption as the contrast between air and matrix is similar to the contrast between air and paraffin, shown in Fig. 5.7. This approach utilised an area at the top of the pore sample that appeared to be unaffected by paraffin throughout the experiment, giving an area which remains static and comparable for all 57 scans. By separating the matrix from the air in this area, one can measure the location of the separation boundary along the same fixed line for all scans. In theory, only random noise and blurring would then cause any differences in the measured location. Doing this for ten different lines for all 57 scans gave the distribution shown in Fig. 5.6, which also gave a standard deviation of 2.4 voxels.

It might be somewhat surprising that the two methods yielded almost identical distributions. Expecting that the first method also would be affected by the displacement of the fluid interface during the 40-second imaging window, causing some additional blur. However, the area used for the second method is further from the centre of rotation. The analysis could therefore be affected by some misalignment between the tomograms and a general blurring effect that occurs as the sample rotates during the 0.5 exposure time for each projection, an effect more predominant further from the centre of rotation. This effect is apparent when examining the metal piece in Fig. 5.3. Nevertheless, one should conclude from the measured distributions that the fluid interface is significantly affected by both noise and blurring, emphasising the use of a mask and fitting smooth surfaces to parts of the fluid interface.

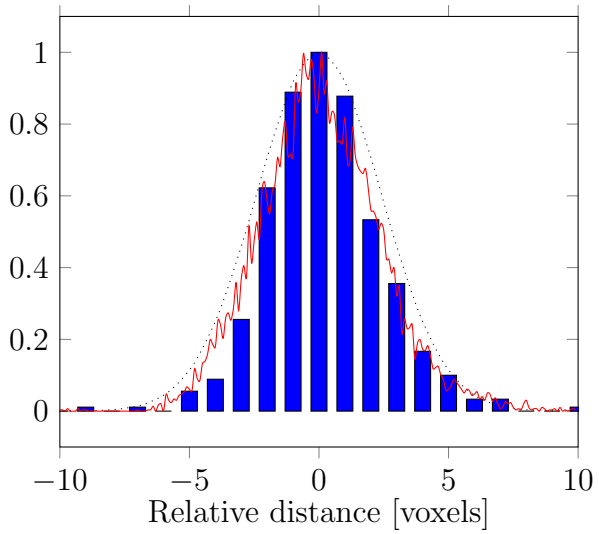

Figure 5.6: Blue represents the distance distribution of the measured boundary points between matrix and air relative to the mean distance. Red represents the distribution of residual distances relative to the fitted surfaces. All plots are normalised, and the dotted black line represents a Gaussian distribution with a mean equal to 0 and a standard deviation of 2.4 voxels.

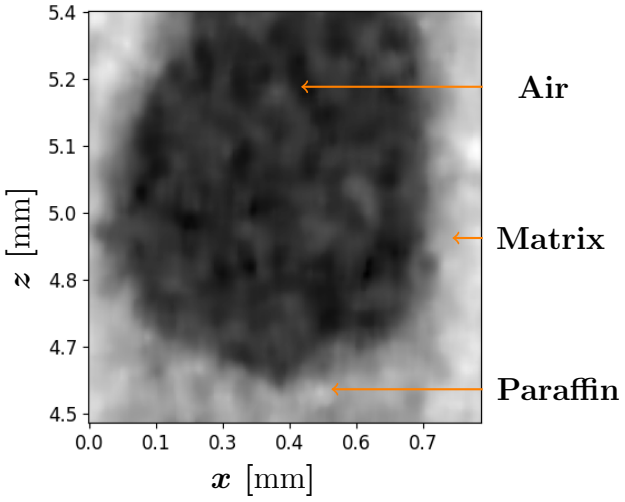

Figure 5.7: Illustrating cross-section of the pore system and the contrast between air, paraffin and matrix.

5.4 Future work

Using X-ray µCT home-lab equipment to capture the evolution of multiphase flow in porous media is a complex task, where several parameters and technical details need to be optimal to maximise the potential of the equipment and gain more insight into the imaged system. While developing the experimental setup and analysing the result, various potential improvements were revealed and should be tested in future experiments.

The flooding setup and the sample are essential to accurately verify the system's capability to obtain a time-resolved data set, as this is linked to the velocities of the fluid-fluid interface. An obvious improvement to this experiment would be to enhance the accuracy of the pump rate, which has to reflect the size, morphology and material of the porous network. Further testing of the pump is then needed to deal with the leakage problem, and only after that would it be natural to reduce the volumetric size of the injectant fluid vessel, directly contributing to a lower pump rate. Apart from the technical details of the pump, it would be beneficial to reduce the complexity of the system for a more robust verification of the flooding setup. This could be achieved by testing different fluids, with potentially higher viscosity, in an alternative sample with simpler geometries, such as a pore channel with a constant width. It could also be an idea to test a more realistic sample with mixed wettability characteristics.

It was evident throughout the imaging process that some of the default settings on the Nikon system hindered an optimal experiment, such as the 20-second delay between each tomogram acquisition and the velocity limit on the rotating stage. There is, however, an inbuilt feature within the Nikon software that allows users to control and manipulate their Nikon X-ray CT system through Inter Process Communication. Utilising this would make it possible to surpass the default settings of the Nikon system. A different and perhaps more innovative approach would be to introduce an independent controllable rotating stage and use the CT system to simply acquire a sequence of radiograms. Subsequently, these radiograms are treated

as projections in the reconstruction process. This would give the experimentalist more control over the process, surpassing unnecessary system settings.

An unavoidable consequence of operating at the limit of fast image acquisition times is the low signal-to-noise ratio, which will reduce the quality of the reconstructed tomograms. It is not given that the standard filter back projection is the optimal algorithm to deal with this. Hence, other algorithms are worth exploring. One such method is an iterative reconstruction algorithm, which some research suggests is more effective when the signal-to-noise level is low[48].

Chapter 6

Conclusion

In this thesis, a two-phase flow system consisting of paraffin and air inside a simplified porous system has been studied by analysing a sequence of tomograms obtained by a Nikon µCT scanner system. The results from the analysis revealed that the obtained dataset describing the evolution of the fluid-fluid interface inside the pore space was constrained by its temporal resolution. The imaging technique was only able to capture a portion of the dynamics fast enough for the data set to be considered fully time-resolved. For this experiment, the criterion for a fully time-resolved data set was met when all measured velocities were below 17 µm/min. As the maximum measured velocity for the IPW-area was measured 12 µm/min and the maximum measured velocity for the displacement front was measured 58 µm/min, it is clear that only the IPW-area could be defined as time-resolved. Despite the temporal limitations of the experiment, it was still able to capture the general movement and development of the fluid interface. The fluid interface was observed to change due to the drainage of paraffin, the morphological structure of the pore space, and the retrograde motion of paraffin along the pore walls. However, the experiment was unable to capture local details of the fluid interface that deviated from a simple parabolic morphology. This limitation was primarily attributed to the lack of temporal resolution.

The findings of this thesis underscore the importance of fast imaging techniques in studying dynamically evolving systems. While improvements to the specific setup used in this experiment are feasible and have been suggested, the results indicate that alternative methods, such as employing a synchrotron as a radiation source, are necessary when dealing with fluid flow velocities in the system of higher orders in magnitude. Consequently, using a µCT scanning system should be primarily limited to the study of relatively slowly changing systems.

Bibliography

[1] Mats-Johan H.Fagerheim. *Optimizing X-ray computed tomography for the Study of fluid flow in porous media: A analysis of projection number and resolution.* 2022.

[2] Jacob Bear. *Dynamics of Fluids in Porous Media.* Courier Corporation, 1988. ISBN: 978-0-486-65675-5.

[3] J. J. L. Higdon. "Multiphase Flow in Porous Media". In: *Journal of Fluid Mechanics* 730 (2013), pp. 1–4. ISSN: 0022-1120, 1469-7645. DOI: 10.1017/jfm.2013.296.

[4] An-Hui Lu and Guang-Ping Hao. *Porous materials for carbon dioxide capture.* 2013. DOI: 10.1039/C3IC90003G.

[5] K. A. Jackson and Bruce Chalmers. "Freezing of Liquids in Porous Media with Special Reference to Frost Heave in Soils". In: *Journal of Applied Physics* 29.8 (1958), pp. 1178–1181. ISSN: 0021-8979. DOI: 10.1063/1.1723397.

[6] Khalil Khanafer and Kambiz Vafai. "The role of porous media in biomedical engineering as related to magnetic resonance imaging and drug delivery". In: *Heat and Mass Transfer/Waerme- und Stoffuebertragung* 42 (2006), pp. 939–953. DOI: 10.1007/s00231-006-0142-6.

[7] Nagi Abdussamie. *Flow and Transport Problems in Porous Media Using CFD.* 2014. DOI: 10.13140/RG.2.2.20333.67048.

[8] Riley E. Alexander and Richard B. Gunderman. "EMI and the First CT Scanner". In: *Journal of the American College of Radiology* 7.10 (2010), pp. 778–781. ISSN: 1546-1440. DOI: 10.1016/j.jacr.2010.06.003.

[9] Takashi Ikeda et al. "Preliminary Study on Application of X-Ray CT Scanner to Measurement of Void Fractions in Steady State Two-Phase Flows". In: *Journal of Nuclear Science and Technology (Tokyo)* 20.1 (1983), pp. 1–12. ISSN: 0022-3131.

[10] Herminso Villarraga-Gómez and Stuart Smith. "Effect of the number of projections on dimensional measurements with X-ray computed tomography". In: *Precision Engineering* 66 (2020), pp. 445–456. DOI: 10.1016/j.precisioneng.2020.08.006.

[11] Theodore Heindel. "A Review of X-Ray Flow Visualization With Applications to Multiphase Flows". In: *Journal of Fluids Engineering* 133 (2011), p. 074001. DOI: 10.1115/1.4004367.

[12] E. A. Zwanenburg, M. A. Williams and J. M. Warnett. "Review of High-Speed Imaging with Lab-Based x-Ray Computed Tomography". In: *Measurement Science and Technology* 33.1 (2021), p. 012003. ISSN: 0957-0233. DOI: 10.1088/1361-6501/ac354a.

[13] P. Spanne et al. "Synchrotron Computed Microtomography of Porous Media: Topology and Transports". In: *Physical Review Letters* 73.14 (1994), pp. 2001–2004. ISSN: 0031-9007. DOI: 10.1103/PhysRevLett.73.2001.

[14] Markus Tuller, Ramaprasad Kulkarni and Wolfgang Fink. "Segmentation of X-Ray CT Data of Porous Materials: A Review of Global and Locally Adaptive Algorithms". In: *Soil-Water-Root Processes: Advances in Tomography and Imaging,* vol. 61. 2013, pp. 157–182. ISBN: 978-0-89118-958-9. DOI: 10.2136/sssaspecpub61.c8.

[15] Simone Carmignato, Wim Dewulf and Richard K. Leach. *Industrial X-Ray Computed Tomography*. 2018.

[16] Thorsten Buzug. *Computed Tomography*. Springer Berlin Heidelberg, 2018.

[17] Shady Hermena and Michael Young. *CT-scan Image Production Procedures*. 2023.

[18] H. A. Kramers. "XCIII. On the theory of X-ray absorption and of the continuous X-ray spectrum". In: *Philosophical Magazine Series 1* 46 (), pp. 836–871.

[19] Gavin Poludniowski et al. "SpekCalc: a program to calculate photon spectra from tungsten anode X-ray tubes". In: *Physics in medicine and biology* 54 (2009), N433–8. DOI: 10.1088/0031-9155/54/19/N01.

[20] Miles V.Klein and Thomas E Furtak. *Optics, Second Edition*. Wiley, 1986. ISBN: 9780471872979.

[21] *Diagnostic Radiology Physics*. Non-Serial Publications. Vienna: INTERNATIONAL ATOMIC ENERGY AGENCY, 2014. ISBN: 978-92-0-131010-1.

[22] M.J. Bergera et al. *XCOM: Photon Cross Sections Database*. en. 2009. URL: https://www.nist.gov/pml/xcom-photon-cross-sections-database.

[23] Bushberg Jerrold et al. *The Essential Physics of Medical Imaging, Third Edition*. LIPPINCOTT WILLIAMS and WILKINS, 2012. Chap. 17.3. ISBN: 9780781780575.

[24] Wenxiang Cong et al. "Monochromatic Image Reconstruction via Machine Learning". In: *Machine learning: science and technology* 2.2 (2021), p. 025032. ISSN: 2632-2153. DOI: 10.1088/2632-2153/abdbff.

[25] Amirkoushyar Ziabari et al. *Beam Hardening Artifact Reduction in X-Ray CT Reconstruction of 3D Printed Metal Parts Leveraging Deep Learning and CAD Models*. 2020. DOI: 10.1115/IMECE2020-23766.

[26] Ozarslan E Koay CG Sarlls JE. *Three-dimensional analytical magnetic resonance imaging phantom in the Fourier domain*. 2007.

[27] Haijo Jung. "Basic Physical Principles and Clinical Applications of Computed Tomography". In: *Progress in Medical Physics* 32 (2021), pp. 1–17. DOI: 10.14316/pmp.2021.32.1.1.

[28] Maria Lyra and Agapi Ploussi. "Filtering in SPECT Image Reconstruction". In: *International Journal of Biomedical Imaging* 2011 (2011), e693795. ISSN: 1687-4188. DOI: 10.1155/2011/693795.

[29] Danyu Li et al. "Time-averaged Spray Analysis in the Near-field Using Broadband and Narrowband X-ray Measurements". In: *Atomization and Sprays* 29 (2019). DOI: 10.1615/AtomizSpr.2019030744.

[30] Nick Brierley, Bethan Nye and John McGuinness. "Mapping the Spatial Performance Variability of an X-ray Computed Tomography Inspection". In: *NDT & E International* 107 (2019), p. 102127. ISSN: 0963-8695. DOI: 10.1016/j.ndteint.2019.102127.

[31] Magnus Bro Kolstø. "Exploring Avenus for Compressed Sensing in X-ray Tomography". MA thesis. NTNU, 2018.

[32] Uwe Zscherpel et al. "Unsharpness Characteristics of Digital Detectors for Industrial Radiographic Imaging". In: *Journal of Nondestructive Testing* 9 (2004).

[33] C.E. Shannon. "Communication in the Presence of Noise". In: *Proceedings of the IRE* 37.1 (1949), pp. 10–21. ISSN: 2162-6634. DOI: 10.1109/JRPROC.1949.232969.

[34] Nobuyuki Otsu. "A Threshold Selection Method from Gray-Level Histograms". In: *IEEE Transactions on Systems, Man, and Cybernetics* 9.1 (1979), pp. 62–66. DOI: 10.1109/TSMC.1979.4310076.

[35] Anwar Shah et al. "Comparative analysis of median filter and its variants for removal of impulse noise from gray scale images". In: *Journal of King Saud University - Computer and Information Sciences* 34.3 (2022), pp. 505–519. ISSN: 1319-1578. DOI: https://doi.org/10.1016/j.jksuci.2020.03.007. URL: https://www.sciencedirect.com/science/article/pii/S131915782030327X.

[36] Bartomeu Coll and Jean-Michel Morel. *A non-local algorithm for image denoising*. 2005. DOI: 10.1109/CVPR.2005.38.

[37] © 2022 Phrozen Technology. *phrozen sonic mini 8k RD printer*. 2022. URL: https://phrozen3d.com/products/phrozen-sonic-mini-8k-resin-3d-printer?variant=43781374345403.

[38] © 2022 Phrozen Technology. *phrozen Aqua 8k Resin*. 2022. URL: https://phrozen3d.com/products/phrozen-aqua-8k-resin?ref=assortion&page=product&pid=7210450387131&oid=daba1a5f-ef9a-476e-b949-f029077dd4e1&variant=41910314533051#specs.

[39] Thermo Fisher scientific. *AVIZO*. URL: https://www.thermofisher.com/no/en/home/electron-microscopy/products/software-em-3d-vis/avizo-software.html.

[40] *MKR WiFi 1010 — Arduino Documentation*. URL: https://docs.arduino.cc/hardware/mkr-wifi-1010.

[41] *X-Ray CT - Nikon Industrial Metrology*. URL: https://industry.nikon.com/en-us/products/x-ray-ct/inspect-x-3d-ct/.

[42] *Exxsol™ D60 Fluid – Union Petrochemical Public Company Limited*. 2022. URL: https://www.unionpetrochemical.com/product/exxsol-d60-fluid/.

[43] Nikon metrology NV. *CT Pro*. URL: https://industry.nikon.com/en-gb/.

[44] Pauli Virtanen et al. "SciPy 1.0: Fundamental Algorithms for Scientific Computing in Python". In: *Nature Methods* 17 (2020). DOI: 10.1038/s41592-019-0686-2.

[45] K. W. Vugrin et al. "Confidence Region Estimation Techniques for Nonlinear Regression in Groundwater Flow: Three Case Studies: CONFIDENCE REGIONS IN GROUNDWATER FLOW". In: *Water Resources Research* 43.3 (2007). ISSN: 00431397. DOI: 10.1029/2005WR004804.

[46] Eric W. Weisstein. *Mean Curvature*. URL: https://mathworld.wolfram.com/MeanCurvature.html.

[47] Pedro Balestrassi et al. "A Multivariate Descriptor Method for Change-Point Detection in Nonlinear Time Series". In: *Journal of Applied Statistics* 38 (2011), pp. 327–342. DOI: 10.1080/02664760903406496.

[48] Ahmed Fareed et al. "Impact of Iterative Reconstruction vs. Filtered Back Projection on Image Quality in 320-Slice CT Coronary Angiography". In: *Medicine* 96.48 (2017). ISSN: 0025-7974. DOI: 10.1097/MD.0000000000008452.

NTNU
Norwegian University of
Science and Technology

SINTEF